

RESEARCH

Open Access



# Single-cell and spatial transcriptomic analyses revealing tumor microenvironment remodeling after neoadjuvant chemoimmunotherapy in non-small cell lung cancer

Xiaolu Cui<sup>1†</sup>, Siyuan Liu<sup>2†</sup>, He Song<sup>3\*</sup>, Jingjing Xu<sup>4\*</sup> and Yanbin Sun<sup>2\*</sup>

## Abstract

Non-small cell lung cancer (NSCLC) represents the most common pathological type of lung cancer, and the combination of neoadjuvant immunotherapy with chemotherapy has emerged as the first-line treatment for NSCLC. Nevertheless, the efficacy of this therapeutic approach remains variable. The present study aims to examine the impact of chemoimmunotherapy in NSCLC patients, with a view to identifying key molecules, critical cell sub-populations, communication patterns and spatial distributions that potentially correlate with therapeutic sensitivity. A total of 16 lung cancer tissue samples were collected from a cohort of 12 NSCLC patients and subjected to single-cell RNA and spatial transcriptome sequencing. Our data demonstrated that the distribution of CD4+Treg T cells and mCAFs indicated an immunosuppressive tumor microenvironment, while the accumulation of CD4+Th17 T cells and iCAFs could act as a positive marker for the sensitivity to chemoimmunotherapy. Furthermore, a significant high level of SELENOP-macrophages was observed in tissues from positive responders, and a strong co-localization between SELENOP-macrophages and antigen-presenting cancer associated fibroblasts (CAFs) in the tumor boundaries was identified, indicating the cooperative roles of these two cell types in response to combined therapy. Moreover, SELENOP-macrophages were observed to be accumulated in tertiary lymphoid structures, which further suggested its critical role in recruiting lymphocytes. Furthermore, analysis of cell–cell communication, based on spatial transcriptomics, suggests that the interactions between SELENOP-macrophages, apCAFs, CD4+ and CD8+ T cells were significantly enhanced in responders. In addition, SELENOP-macrophages recruited CD4+ Naïve, Helper and CD8+ Naïve T cells through pathways such as the cholesterol, interleukin, chemokine and HLA when responding to combined therapy. The present study further unveils the dynamic spatial and transcriptional changes in the tumor microenvironment of non-small cell lung cancer in response to combination therapy.

<sup>†</sup>Xiaolu Cui and Siyuan Liu contributed equally to this work.

\*Correspondence:

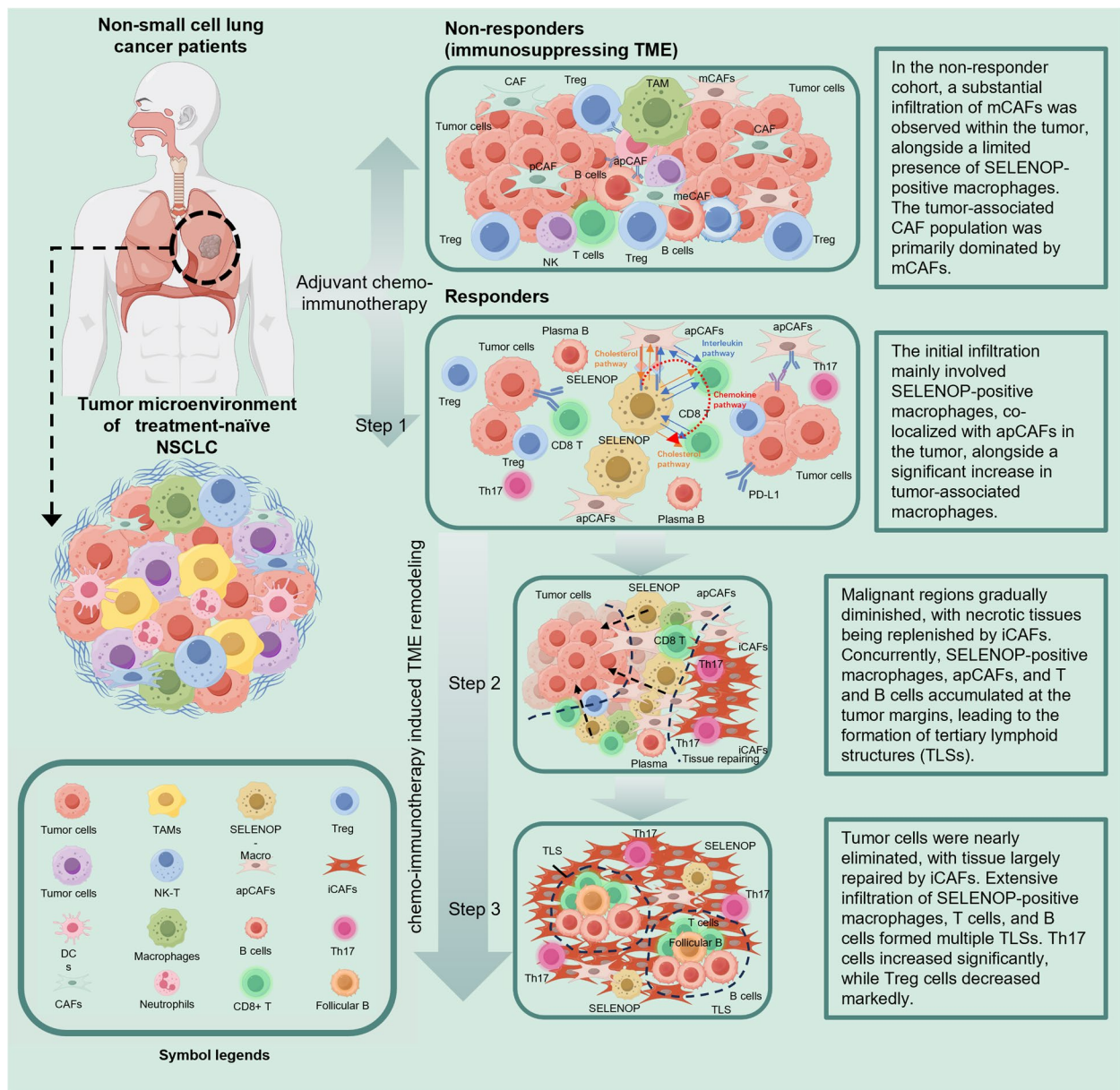
He Song  
hsong@cmu.edu.cn  
Jingjing Xu  
xujj@cmu.edu.cn  
Yanbin Sun  
ybsun@cmu.edu.cn

Full list of author information is available at the end of the article



**Keywords** Non-small cell lung cancer, Single-cell RNA sequencing, Spatial transcriptome, Neoadjuvant chemoimmunotherapy, Tertiary lymphoid structures

**Graphical Abstract**



**Introduction**

Lung cancer is the leading cause of death for cancer patients worldwide, accounting for 20% of all cancer-related deaths [1, 2]. Lung cancer is the second most common cancer in terms of the estimated number of new cancer cases in 2024 [1]. Non-small cell lung cancer

(NSCLC) accounts for 85% of all lung cancer cases [3], adenocarcinoma accounts for approximately 40%, and squamous cell carcinoma accounts for 25–30% of all lung cancer cases. Over the past decade, immunotherapy has changed the treatment landscape for NSCLC [4, 5]. Immune checkpoint blockade (ICB) has significantly

extended progression-free survival (PFS) and overall survival (OS) in patients with stage III NSCLC, with a high response rate (RR) [6, 7]. Notably, combination chemoimmunotherapy has shown greater treatment efficacy than chemotherapy alone does, and this combination treatment strategy benefits patients with both nonsquamous and squamous cancers, regardless of the expression status of programmed cell death ligand 1 (PD-L1) [8, 9]. Immunotherapy has become the first-line treatment for NSCLC, and neoadjuvant immunotherapy before surgical resection in patients with resectable NSCLC has resulted in longer event-free survival and a higher rate of pathological complete response [10, 11]. Nonetheless, a proportion of patients remain unresponsive to ICB, and the mechanisms of immunotherapy resistance are poorly understood.

In addition to PD-L1 expression levels, several factors can predict the response to immunotherapy in cancer patients, including alterations in genomic signature genes, tumor mutation burden and the status of distinct T-cell subtypes [12–15]. The tumor microenvironment (TME) plays a critical role in tumor progression, metastasis and sensitivity to anticancer therapy [14, 16]. The TME is a highly heterogeneous ecosystem containing a variety of cellular components, including immune cells, fibroblasts, endothelial cells and epithelial cells. The intricate interactions between immune cells and cancer-associated fibroblasts, malignant epithelial cells and endothelial cells are essential for the remodeling of the TME, including immune activation, immune escape, extracellular matrix (ECM) remodeling and tumor metastasis [17, 18]. ICB is capable of reshaping the TME, and the remodeled TME can evolve in different directions, such as enhanced therapeutic sensitivity or induced therapeutic resistance, ultimately leading to different therapeutic outcomes, i.e., pathological complete response (pCR) of the tumors or immune escape and therapeutic resistance [19, 20]. ICB in combination with chemotherapy has become a first-line treatment option for early-stage NSCLC patients before surgical resection, and clinical trial data have confirmed that neoadjuvant chemoimmunotherapy can significantly increase the rates of major pathological response (MPR) and pCR [8, 10, 21]. However, the effects of immune checkpoint blockade on the re-establishment of the TME in NSCLC and how the altered responsiveness of the TME to ICB affects the course of treatment response are not well characterized.

Recently, studies have focused on the dynamic changes in the TME in response to immunotherapy and analyzed the associations between TME remodeling and the clinical outcomes of immunotherapy. As a predominant cytotoxic cell component in the TME, clonal expansion and infiltration of T cells have been shown to be positive responses to ICB

therapy, among which specific subtypes of T cells, such as CD137+CD8+T cells, PD-1+Ki-67+CD8+T cells and Tregs, have been found to predict the response to neoadjuvant chemoimmunotherapy in NSCLC patients [12, 13, 22]. Tumor-infiltrating B (TIB) cells have also been associated with the therapeutic responsiveness of immunotherapy in NSCLC, and among the B-cell subtypes, memory B cells with G protein-coupled receptor 183 have been found to be correlated with a positive therapeutic response [23]. The number of tumor-infiltrating neutrophils increases after successful immunotherapy, and therapy-induced neutrophils, which require an interferon gene signature, are essential for an effective response to immunotherapy [24]. In NSCLC, Hui et al. investigated immune cell profiles after neoadjuvant chemoimmunotherapy via single-cell RNA sequencing (scRNA-seq) and reported that several critical events, including the inhibition of activated TNFRSF4 regulatory T cells (Tregs), increased LAMP3 dendritic cells (DCs), and the expansion of intratumoral CD4 T clones and peripheral C3 cytotoxic CD8 T clones, were correlated with positive clinical outcomes [19]. They focused mainly on immune cell changes in their study. Hu et al. provided a more comprehensive analysis of TME changes, including malignant epithelial cells and key immune cells, after neoadjuvant chemoimmunotherapy in NSCLC patients [20]. They also compared the scRNA-seq data from patients with MPR or non-major pathological response (NMPR) after treatment and reported significant changes in T cells, B cells, macrophages, neutrophils and cancer cells. However, owing to the limitations of scRNA-seq in these studies, their analysis did not include changes in the spatial distribution of cells, which are likely closely linked to the response to immunotherapy. In addition, the focus of their study was on immune cells, and although they discussed the changes in the fraction of malignant epithelial cells after combination therapy, they did not provide in-depth insight into the differentiation of malignant epithelial cells and their communication with other cell types.

To gain insight into the dynamic changes in the tumor microenvironment of non-small cell lung cancer patients following neoadjuvant chemoimmunotherapy, we conducted comprehensive and in-depth single-cell RNA sequencing and spatial transcriptome sequencing on tumor tissue samples from a cohort of 12 NSCLC patients who underwent surgically resection of the tumors in our center. The validation cohort including two independent cohorts of NSCLC patients was also employed to validate some of the findings. This study aimed to investigate the changes in gene expression patterns, biological functions, cell development and interactions among immune cells, stromal cells and malignant cells in response to the therapy.

## Materials and methods

### Patient cohorts and tissue collection

A total of 12 patients were included in this study, all of whom underwent surgical resection of the tumors at the Department of Thoracic Surgery, First Hospital of China Medical University, from January 2022 to March 2023 and were pathologically diagnosed with NSCLC (Table S1a). Informed consent was obtained from each patient prior to sample collection, and the study was approved by the Ethics Committee of China Medical University (Authorization number: AF-SOP-07-1.2-01). Patient inclusion criteria was as follows: (1) Age from 50 – 80 years old. (2) Underwent percutaneous lung tumor biopsy before surgery and were diagnosed with NSCLC. (3) Written informed consent was obtained from each patient for both surgery and research purposes. (4) The enrollment of the patients complied with the ethical requirements by ethics committee of First Hospital of China Medical University. Among them, six patients received 3–5 cycles of neoadjuvant immunotherapy (PD-L1 blockade) combined with cisplatin-based chemotherapy prior to surgery, and are categorized as the post-treatment (PT) group, whereas the other six patients received thoracoscopic lobectomy without any neoadjuvant therapy, and these patients are categorized as the treatment-naïve (TN) group. All patients who received neoadjuvant therapy showed a significant reduction in tumor volume by computed tomography (CT) imaging, and the final pathological diagnosis was as follows: non-major pathologic response in 3 patients, major pathological response ( $\leq 10\%$  residual viable tumor in the primary tumor and lymph nodes) in 2 patients and pathologic complete response (0% residual viable tumor in the primary tumor and lymph nodes) in 1 patient [25, 26]. In all cases, fresh lung tumor tissue was collected immediately after surgical resection for tissue processing and scRNA-seq. Additionally, in order to identify the reshaping of NSCLC tumor microenvironment by neoadjuvant therapy, formalin-fixed paraffin-embedded (FFPE) sections from four patients with pathological assessments from NMPR to pCR in the neoadjuvant cohort were collected for spatial transcriptome sequencing.

For the two patients (patient 08 and patient 09) evaluated as NMPR, their tumor tissue samples were able to demonstrate the characteristics of a “cold” tumor microenvironment that was unresponsive to neoadjuvant therapy. In contrast, although patient 12 was evaluated as NMPR, we observed a significant boundary between the malignant regions and non-malignant structures in the tumor sections by hematoxylin–eosin (H&E) staining. Therefore, the tissue sample from patient 12 should reflect the characteristics of the tumor microenvironment that was in the process of responding

to neoadjuvant therapy. Finally, the samples from the patient evaluated as pCR (patient 10) were able to reflect the characteristics of the tumor microenvironment that had reached a complete pathological response after neoadjuvant therapy. These four tumor samples should be able to reflect the different sensitivities of NSCLC tumors in response to neoadjuvant therapy, alongside the different stages of the tumors in the process of responding to neoadjuvant therapy. Hence, they were selected for spatial transcriptome sequencing.

FFPE sections from a cohort of 10 NSCLC patients who underwent surgical resection of the tumors at the Department of Thoracic Surgery, First Hospital of China Medical University were collected for validation. Among them, 6 patients received 3–5 cycles of neoadjuvant immunotherapy (PD-L1 blockade) combined with cisplatin-based chemotherapy prior to surgery. The final pathological diagnosis for the post-treatment patients was as follows: NMPR in 3 patients, MPR in 1 patient and pCR in 2 patients (Table S1b).

### Tissue dissociation and scRNA-seq

Fresh NSCLC tumor tissues were obtained from patients, washed with ice-cold phosphate-buffered saline (PBS) and processed with a tumor dissociation kit (Miltenyi Biotec, Germany) to prepare single-cell suspensions. Cellular suspensions were loaded on a 10X Genomics Gem-Code single-cell instrument that generates single-cell gel bead-in-EMLusion (GEMs). Libraries were generated and sequenced from the cDNAs with Chromium Next GEM Single Cell 5' Reagent Kits v3. Barcoded, full-length cDNAs were then reverse-transcribed from polyadenylated mRNAs to generate sufficient masses for library construction, which were sequenced on an Illumina NovaSeq 6000 platform at Gene Denovo Biotechnology (Guangzhou, China).

### Data quality control and gene expression quantification

Genome alignment was performed via 10X Genomics Cell Ranger software (version 6.1.0). Following alignment, briefly, cells meeting the following criteria were retained through Seurat (Version 3.0) and were passed to downstream analysis: (1) nFeature range from 300 to 6500; (2) 600 to 43,000 unique molecular identifiers (UMI)s; (3)  $< 15\%$  UMIs of mitochondria genes. Potential doublets and multiplets were filtered by DoubletFinder to avoid influencing cell clustering and annotation. After quality control, the gene expressions were normalized by Seurat LogNormalize, which is a global-scaling normalization method [27]. Subsequently, Harmony algorithm was used to integrate all samples, minimizing batch effect. Principal component analysis was then carried

out on the integrated expression matrix for dimensional reduction and downstream analysis.

### Cell clustering and annotation

The integrated expression matrix is then scaled, and principal component analysis (PCA) is performed for dimensional reduction. Then, we implemented a resampling test inspired by the jackStraw procedure. We identified 'significant' PCs as those with strong enrichment of genes with low  $p$  values for downstream clustering and dimensionality reduction. The distances between the cells were calculated on the basis of previously identified PCs. The log-normalized matrices were then loaded on SingleR R packages (version 1.8.1) for cell type annotation and verified by manual annotation, which was based on correlating the gene expression of reference cell types with single-cell expression.

### Differentially expressed gene analysis

The expression values of each gene in a given cluster were compared against those of the remaining cells via the Wilcoxon rank sum test. Significantly upregulated genes were identified via several criteria. First, genes had to be at least 1.28-fold overexpressed in the target cluster. Second, genes had to be expressed in more than 25% of the cells belonging to the target cluster. Third, the  $p$  value is less than 0.05.

### Differentially expressed gene analysis for groups

Seurat (version 4.1.0) was used for differentially expressed gene analysis. New individuals were set up as "group\_cluster" or "group\_cell type" for analysis. We subsequently used a hurdle model in MAST (Model-based Analysis of Single-cell Transcriptomics) to identify differentially expressed genes for a group in one cluster. We identified differentially expressed genes (DEGs) according to the following criteria: 1)  $|\logFC| \geq 1$ ; 2)  $p\_value\_adj \leq 0.05$ ; and 3) the percentage of cells where the gene was detected in a specific cluster was greater than 10%.

### Single-cell V(D)J analysis

After GEM generation, the gel beads are ruptured, and the cells are lysed. GEMs are then incubated, and polyA mRNA in cell lysates is reverse transcribed to generate barcoded full-length first-strand cDNA. The cDNA was then purified and amplified via PCR. The cDNA product was then purified and subjected to subsequent T-cell and B-cell enrichment. Before constructing the library, the enriched V(D)J fragments were digested and screened to generate DNA fragments of different lengths. An Illumina sequencing library with V(D)J enrichment and 5' gene expression was constructed via the single-cell V(D)J Kit. Sequencing was performed via an Illumina NovaSeq

6000 at Gene Denovo Biotechnology (Guangzhou, China). We used Trust4 software to analyze the bioinformatics data, construct an immune library, and visualize the analysis results.

### Spatial transcriptomics (ST)

ST was performed via the Visium Spatial Gene Expression System (10×Genomics). We first performed RNA quality control and trimming on paraffin-embedded blocks of lung cancer tissue, and then the sections were prepared at room temperature at a thickness of 5  $\mu\text{m}$  and subjected to deparaffinization, HE staining, 85% glycerol sealing and brightfield imaging experiments. Next, we used probe hybridization to detect transcripts. The probe hybridization system uses the RTL (RNA-templated ligation) technique, where each gene is detected via two probes, the left arm and the right arm. Then, the polyA end of the DNA strand can be captured by binding to the poly(dT) of the capture sequence, and the read2 end provides the binding site for the amplification primer, which completes the amplification of the DNA with barcode information. DNA with barcode information is amplified. Once the probes have been purified, library construction begins. The mRNA in the tissue is degraded via RNase, which releases the probe, which hybridizes to the mRNA. The polyA of the probe was attached to the poly(dT) of the capture sequence on the chip, and PCR amplification was performed using read2 sequences to extend the probe, allowing the probe to be coupled with the barcode sequence and the UMI sequence. We then used 0.08 M KOH in an alkaline environment to break the hydrogen bond between the extended probe and the capture sequence, and the probe with the labeled sequence could be transferred from the solid-phase vector to the liquid-phase system to facilitate subsequent library construction. Single-stranded DNA is amplified by PCR to increase its abundance and added to the sequencing junction to complete library construction. The cDNA libraries were sequenced on the Illumina sequencing platform by Genedenovo Biotechnology Co., Ltd. (Guangzhou, China). Alignment and demultiplexing were conducted via the Space Ranger pipeline, and subsequent analyses were conducted via Seurat (version 4.2.0) in R. We obtained the expression abundance information of different genes in different spots on the basis of the genome comparison results, UMI counts and barcode sequence information.

Before spot clustering, the data were normalized for more accurate clustering. We employ a normalization algorithm "SCTransform" that normalizes the gene expression for each spot in a regression model with a negative binomial error distribution and log link function. The primary function of the SCTransform algorithm

is to perform data pre-processing and normalization on spatial transcriptome data. It is employed to reduce technical noise, correct the batch effects and provide reliable and comparable data for subsequent analysis. To overcome the extensive technical noise in any single gene for ST data, Seurat clusters spots on the basis of their PCA scores, with each PC essentially representing a 'meta-gene' that combines information across a correlated gene set. We used MAST (Model-based Analysis of Single-cell Transcriptomics) to find differential expression for a single cluster compared with all the other clusters. We identified DEGs according to the following criteria: 1)  $p$  value  $\leq 0.01$ . 2)  $\log_2FC \geq 0.360674$ . 3) The percentage of cells where the gene is detected in a specific cluster  $> 25\%$ . We further selected the top 20 genes as the marker genes according to the results of the differentially expressed genes per cluster. The expression distribution of each marker gene was subsequently demonstrated via a heatmap, t-distributed stochastic neighbor embedding (t-SNE) distribution and bubble diagram.

#### Correlation analysis of the two omics methods

For the single-cell transcriptome, we calculated the average gene expression in each sample. For the spatial transcriptome, we calculated the average amount of gene expression in each slice. We then calculated Pearson correlations between samples of the single-cell transcriptome and slices of the spatial transcriptome. Pearson correlation was used to measure the correlation between omics data.

#### Spot deconvolution

We used a residual convolutional neural network with the transformer decoder (RCTD) tool to predict the cell composition of each spot on the basis of the single-cell transcriptome data. We then used heatmaps, tissue maps, and Circos maps to visualize the distributions of different cell types in the tissues.

#### Identification of malignant cells

Gene expression data and cell type annotations extracted from the Seurat object were used as inputs in the InferCNV package to detect copy number variations (CNVs) and recognize malignant cells. Endothelial cells containing nonmalignant-derived cells were used as the control group. To reduce the possibility of false positive CNV calls, the default Bayesian latent mixture model was implemented to identify the posterior probabilities of alterations in each cell. Low-probability CNVs were filtered using the default value of "0.5" for the threshold. Cells with consistent patterns of CNV were partitioned into groups via the default hierarchical clustering ward.D2.

#### Multiplex immunohistochemistry (mIHC) analysis

mIHC analysis was performed via a Quadruple-Fluorescence Immunohistochemical Mouse/Rabbit Kit (pH 9.0) following the manufacturer's protocol (ImmunoWay, Wuhan, China). The 9A working solution was placed in the repair cartridge and heated until boiling. The paraffin sections were subsequently placed into boiling reagent 9A working solution, heated for 30 min, and then cooled at room temperature. After the sections were removed, 50–100  $\mu$ l of Reagent B was added to the sections, which were incubated at room temperature for 15 min and then rinsed with PBST for 2 min 3 times. The sections were then removed, and the tissues were collected with an immunohistochemistry pen. Then, the corresponding primary antibody was added, and the samples were incubated at 37 °C for 1–2 h. Next, the tissues were rewarmed at 37 °C for 30 min and rinsed with PBST 3 times for 2 min each. The slides were dried, and 50–100  $\mu$ l of Reagent C working solution was added. The slides were incubated at room temperature for 30 min and then rinsed with PBST 3 times for 2 min each. Subsequently, 50–100  $\mu$ l of fluorescent dye reagent D-594 working solution was added. Following a 10-min interval, the sections were rinsed with PBST for 2 min 3 times and then placed in the repair box, and reagent F was added. The sections were incubated in a microwave oven at high power for three minutes. Once cooled, the sections were rinsed with PBST 3 times for 2 min each. The aforementioned steps were repeated, with the intermediate fluorescent dye changed to Reagent D-488, and the slides were labeled with a second primary antibody. Steps 6–9 were repeated, the intermediate fluorescent dye was replaced with Reagent D-647, and the mixture was incubated with the third primary antibody. Steps 6–8 were repeated, the intermediate fluorochrome was replaced with Reagent D-525, and the mixture was incubated with the fourth primary antibody. Then, 30–50  $\mu$ l of Reagent G was added to the sections. After that, the sections were scanned via a Panoramic MIDI digital scanner (3D Histech, Hungary), and the software used for analysis of the pathology results was SlideViewer\_2.5\_RTM\_v2.5.0.143918. Antibodies against CD68 (YM6022), PanCK (YM6815), CXCL9 (YT6008), and SPP1 (YT3467) were purchased from ImmunoWay (Wuhan, China).

#### Immunohistochemistry (IHC) staining

The expression of indicated proteins in NSCLC tissue specimens was detected using an UltraSensitive™ SP (Mouse/Rabbit) IHC kit (Maxin-Bio, Fuzhou, Fujian, China) according to the manufacturer's instructions. Briefly, sections were dewaxed in xylene and ethanol, and antigen retrieval was performed using a microwave for 10 min at 100°C. The sections were then incubated

with antibodies for 1 h, followed by biotinylated anti-IgG antibody and streptavidin-biotinylated-complex horseradish peroxidase. DAB and hematoxylin were used for nuclear staining. The antibodies were as listed as follows: STAT3 (RM8010), STAT5 (RM0478), IL-2 (BD-PE0366), Beta Catenin (RM1224), TGF-beta (RM3267), E2F1 (RM4981). The antibodies were all purchased from Biobio (Suzhou, China).

#### Cell–cell interaction analysis

CellPhoneDB V5 software was used to conduct the cell–cell interaction analysis. The software uses a single-cell gene expression matrix to predict the abundant ligand–receptor interactions between two cell states according to the expression of receptors in one cell type and ligand expression in another cell type and then analyzes the number of ligand–receptor pairs in the cell pair and their expression abundance information. On the basis of the results of the expression abundance and significance  $P$  value of ligand–receptor pairs in each cell pair, we further screened the number of significant ligand–receptor pairs in each cell pair; thus, the communication relationships between cells can be evaluated globally. To evaluate whether a pair of matching receptors is significant, we screened them with a  $P$  value  $\leq 0.05$ , calculated the product of ligand gene expression and receptor gene expression, and then sequenced them from large to small.

#### Gene signature estimation

To estimate the cytotoxic and exhausted signatures of T cells and NK cells, we calculated the cytotoxic score and exhaustion score for each cell via the canonical cytotoxic (GZMA, GZMB, GZMK, GNLY, IFNG, PRF1, and NKG7) and exhausted (LAG3, TIGIT, PCCD1, HAVCR2, CTLA4, LAYN, and ENTPD1) markers, respectively. With the same method, we estimated the phenotypes (M1 or M2) and functions of angiogenesis and phagocytosis for each macrophage with previously reported markers (Table S11). In addition, the antigen processing and presentation signatures of apCAFs were calculated via the same method (Table S11). The mean value of the module scores of a cell cluster ( $\geq 10$  cells) from an individual sample was calculated to present the signature level.

#### Functional enrichment analysis

Pathway enrichment analysis was performed to investigate the pathways and biological processes enriched in different cell types. The significantly upregulated genes of the cell subtypes were identified by comparing the gene expression in a given cluster with that in the remaining cells via the Wilcoxon rank-sum test. The cutoff criteria were set as a fold change  $> 1.28$  and an adjusted

$p$  value  $< 0.05$ . The upregulated genes were subjected to GO enrichment analysis and Kyoto Encyclopedia of Genes and Genomes (KEGG) analysis. In addition, gene set enrichment analysis (GSEA) of a given cell type was conducted with software (<http://software.broadinstitute.org/gsea/index.jsp>). Moreover, we performed gene set variation analysis (GSVA) via a collection of gene sets from MSigDB to identify pathways and cellular processes enriched in different clusters. GSVA was performed as implemented in the GSVA R package version 1.26 on the basis of the cluster-averaged log-transformed expression matrix.

#### Trajectory analysis

##### RNA velocity analysis

The RNA velocity analysis was performed via the package *velocity* (v0.17.13) with the default parameters, and the BAM files were used as inputs. For visualization, velocity vectors were plotted as locally average vector fields on the tSNE embeddings of our high-quality cells from the previous step.

##### Monocle2 pipeline

We used Monocle2 (version 2.22) to perform dimension reduction of the gene expression matrix and construct the differentiation trajectory of the cell clusters. The cells are organized into a tree-like trajectory that includes branches and nodes. The most primitive cell clusters of the differentiation state along the trajectory are subsequently defined as the cell clusters with the smallest pseudotime values, after which the pseudotime values for all the cells are calculated. Genes that are differentially expressed with different differentiation states are filtered out. The genes whose filtering threshold was set to an FDR  $< 1e-5$  were selected as differentially expressed genes. To identify genes with different expression patterns between two branches, negative binomial generalized linear models are fitted to each branch, and differentially expressed genes dependent on different branches are computed and tested. The filtering threshold was set to FDR  $< 1e-7$ .

##### Monocle3 pipeline

We used Monocle3 (version 1.3.1) to divide different cell clusters into different differentiation partitions on the basis of potential differentiation relationships. We used a simple principal tree algorithm, “simplePPT,” to construct individual trajectories and calculate pseudotime values, achieving simultaneous construction of multiple differentiation trajectories. The pseudotime values calculated by Monocle3 and the differentiation partition information are mapped to the original UMAP graph in Seurat.

### Slingshot pipeline

We used Slingshot (version 2.2.0) to identify the lineages of the cell clusters and construct trajectories for the cell clusters. Slingshot identified lineages of cell clusters on a two-dimensional space via a minimum spanning tree (MST), which determines the number of lineages and branches. Differentiated lineages have different endpoint cell clusters but share a common starting cell cluster. Using simultaneous principal curves and orthogonal projection, Slingshot subsequently fits each differentiation lineage on a two-dimensional space and calculates the corresponding pseudotime values for the cell clusters, resulting in multiple linear cell differentiation trajectories originating from a common starting cell cluster. Pseudotime value mapping can map the pseudotime values and differentiation trajectories of cell clusters on different differentiation trajectories.

### Statistics

All the statistical analyses and presentations were performed via R software (version 4.1.3). All the statistical tests used are defined in the figure legends. Statistical significance was set at  $P$  or adjusted  $P < 0.05$ .

## Results

### High-resolution single-cell and spatial transcriptomic analyses characterized the TME landscape of NSCLC patients after adjuvant chemoimmunotherapy

The freshly collected NSCLC samples were immediately digested into a single-cell suspension, and all single-cell transcriptomes were generated via the commercial BD Rhapsody platform. FFPE samples were collected and subjected to spatial transcriptomic analysis. The overall design and patients enrollment in this study were shown in Fig. 1A. The detailed technical processes, including the steps of quality control and filtering, are presented in the Methods and Materials. A total of 58,210 cells with a median of 4887 genes per cell passed quality control and were subjected to further analysis (Figure S1A, S1B, Table S2). All the cells were annotated into 8 cell types according to the well-recognized marker genes by the dimensional reduction method of  $t$ -distributed stochastic neighbor embedding ( $t$ -SNE): T-NK cells, B-plasma cells, endothelial cells, epithelial cells, fibroblasts, mast cells, myeloid cells, and smooth muscle cells. The distributions of cells in different cell types (Fig. 1B), TN/PT groups (Figure S1C) and each patient (Figure S1D) and the distribution of UMIs (Figure S1E, Table S3) are shown by  $t$ -SNE maps. The expression patterns of the common marker genes for each cell type are shown in Fig. 1C, and the selected marker genes are also shown in  $t$ -distributed stochastic neighbor embedding ( $t$ -SNE) maps (Figure S1F). The fractions of the cell clusters in

each patient showed strong heterogeneity (Fig. 1D). In PA04, the fraction of myeloid cells was the highest (2704 cells, 44.62%), whereas in PA07 (MPR), PA10 (pCR) and PA11 (MPR), the levels of epithelial cells were notably decreased (0.69%, 0.65%, and 0.18%, respectively), which is consistent with the pathological assessment. By comparing the numbers and fractions of cell types between the TN and PT groups (Fig. 1E, Figure S1G, Table S4), we found that the number of fibroblasts significantly increased after chemoimmunotherapy. Additionally, in the PT group, the proportions of T-NK cells and mast cells tended to increase, whereas the proportion of epithelial cells tended to decrease (57.76% vs 40.86%, PT vs TN). Notably, in PA10, the only pCR patient, there was a significant increase in the proportions of B-plasma and T-NK cells, the sum of which reached 90%.

To characterize the transcriptomic landscape of the tumor tissues after chemoimmunotherapy, FFPE sections from 4 patients (PA08, PA09, PA10, and PA12) were sampled for spatial transcriptome analysis via the Visium ( $10\times$ Genomics) platform. The computed tomography (CT) images before and after chemoimmunotherapy were used to identify the tumors at baseline and after treatment (Fig. 1F). Upon filtering out the mitochondrial protein-coding genes, the resulting dataset consisted of 12,741 individual spots, with an average of  $\sim 7,651$  genes and  $\sim 7,500$  UMIs per spot. The fraction of spots in each section, the distributions of spots in each cluster and section, and the numbers of UMI counts in each spot were inferred and are shown in the Supplementary files (Figure S2A to S2D).

We performed correlation analyses on sample data from the single-cell transcriptome and spatial transcriptome (Figure S2E). Next, a residual convolutional neural network with transformer decoder (RCTD) algorithm was employed to annotate each spot with cell types on the basis of the integrative analysis of the scRNA-seq and ST data (Figure S2F to Figure S2L). The spatial atlas of major cell types in the NSCLC sections inferred by the RCTD algorithm, as well as the H&E staining of the sections, is shown in Fig. 1G. The cellular composition of each section was also characterized (Fig. 1H). The fraction of epithelial cells in PA08 (tumor-1) and PA09 (tumor-4) was dramatically expanded; in contrast, in PA10 (tumor-2), the predominant cellular components were B-Plasm cells (20.04%) and fibroblasts (35.28%). In PA12 (tumor-3), the proportion of myeloid cells was the highest, accounting for 25.22%, and the proportion of epithelial cells was significantly lower than that in PA08 and PA09, which was replaced by an increased proportion of fibroblasts. The proportions of epithelial cells and immune cells in PA12 were intermediate between those in the NMPR samples (PA08 and PA09) and the pCR

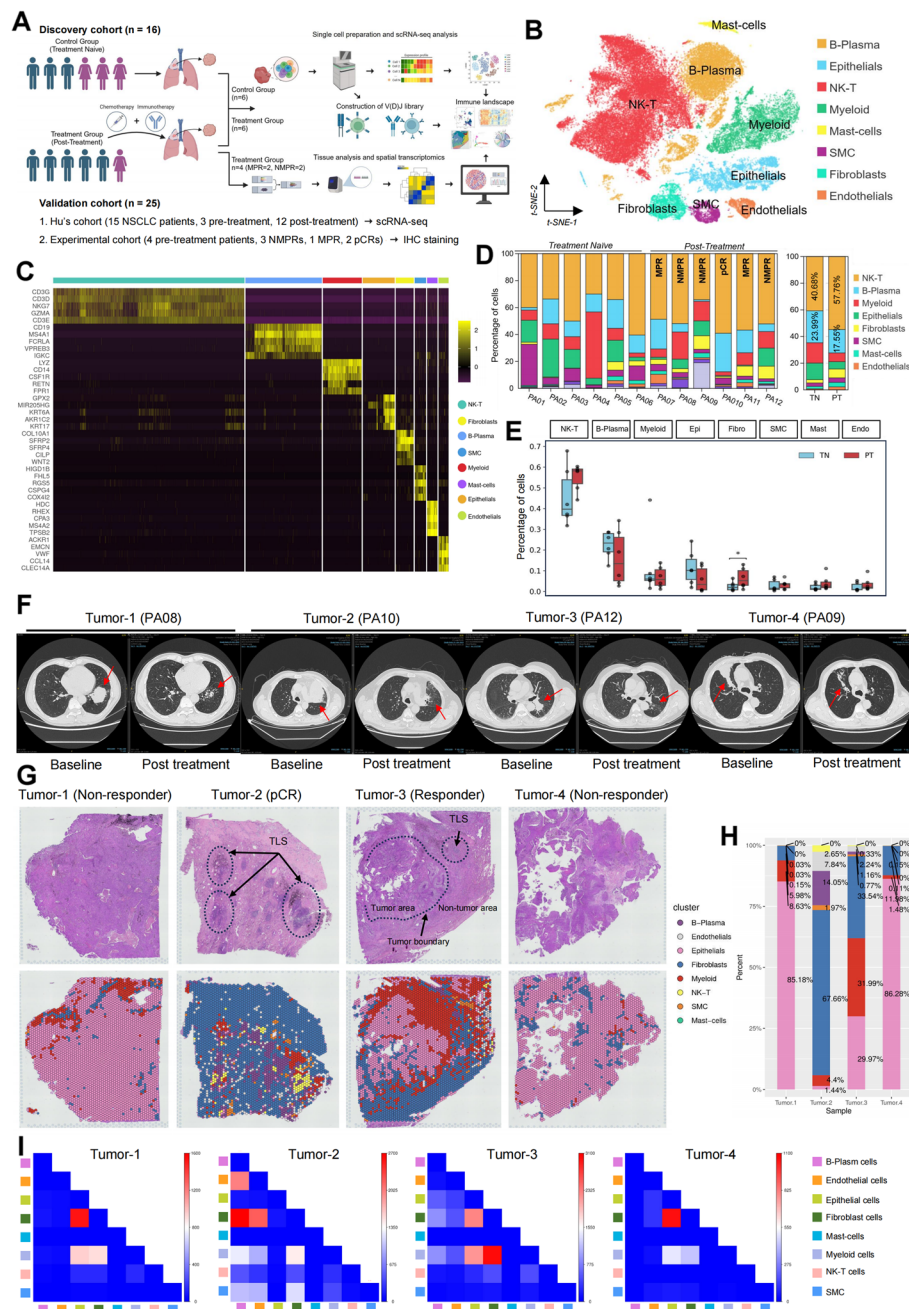


**Fig. 1** High-resolution single-cell and spatial transcriptomic analyses characterized the TME landscape of NSCLC patients after adjuvant chemoimmunotherapy. **A** Overview of sample collection and analysis pipeline, created in biorender (agreement number: OZ267FB6PD). **B** t-SNE plot showing the distributions of 8 distinct cell types from all NSCLC samples. **C** Heatmap showing the marker genes for each cell type in this study. **D** Bar plot showing the distribution of different cell types in each patient and each group. MPR: major pathologic response, NMPR: nonmajor pathologic response, pCR: pathologic complete response. **E** Comparison of the cell fraction between TNs and PTs by Wilcoxon signed-rank test; \* indicates statistical significance. **F** CT images before and after chemoimmunotherapy from PA08, PA09, PA10, and PA12. Red arrows indicate the tumor regions. **G** The spatial annotation of 8 cell types in 4 NSCLC tumor sections inferred by the RCT algorithm (lower), as well as the relative H&E staining (upper) of the sections. The black arrows in the H&E-stained sections indicate the TLS region. TLS: tertiary lymphoid structure. **H** Bar plot showing the percentages of different cell types annotated in the NSCLC sections. **I** Neighboring analysis showing the colocalization relationships between different cell types annotated in the NSCLC sections. Red indicates a close distance between cell types

sample (PA10). Therefore, we assumed that the tumor tissue of PA12 was in a therapy-responsive state, which was in agreement with our observations obtained by H&E staining. In addition, the spatial distribution of the PA12 cells revealed that the epithelial cells were confined by myeloid cells, lymphocytes and stromal cells, which further supported that tumor-3 is a therapy response region. As in tumor-1 and tumor-4, the tissues were dominated by epithelial cells, and only a small number of T-NK cells and myeloid cells infiltrated the tissues. Overall, we defined tumor-1 and tumor-4 regions as immunotherapy-unresponsive regions (non-responders), tumor-2 regions as pCR regions and tumor-3 regions as immunotherapy-responsive regions (responders).

Recent studies have highlighted the importance of tertiary lymphoid structures (TLSs) in antitumor immunity [28, 29], as TLSs are composed of tumor-infiltrating lymphocytes and feature germinal centers, which are commonly observed in secondary lymphoid organs. TLSs are typically defined as an organization of infiltrating lymphocytes in nonhematopoietic organs triggered by chronic inflammation, including cancer, and the existence of TLSs has been associated with favorable prognoses and better responses to immunotherapy [28–30]. In tumor-2, T-NK cells and B cells were found to be significantly infiltrated and organized in several regions, which could be observed as distinct discrete entities by H&E staining; therefore, the regions were identified as TLSs (Fig. 1G). The presence of TLSs in tumor-2 further confirmed that the section is an immunotherapy-responsive region, whereas no TLS regions were observed in the tumor-1 and tumor-4 sections, which were identified as non-responders. Furthermore, the Stereoscope algorithm was used to visualize the distribution of all cell types in TLS-positive sections and TLS-negative sections, from

which we observed notable enrichment of NK-T cells and B cells in the TLS regions (Figure S3A to Figure S3F).

By establishing the spatial architectures of the tumor tissues, we then performed neighboring analysis of major cell types (Fig. 1I). The results revealed that in tumor-1 and tumor-3, myeloid cells colocalized with T-NK cells, and epithelial cells spatially colocalized with myeloid cells and T-NK cells. In tumor 2, B-plasma cells are spatially close to myeloid cells and fibroblasts. Epithelial cells neighbor fibroblasts in tumor-1 and tumor-4. The neighboring relationships between different cell types indicate potential interactions between them. In conclusion, the results of the ST analysis revealed that the tumor tissues exhibited diverse cellular architectures, and the TME landscapes from the NSCLC sections showed a dynamic change in response to chemoimmunotherapy.

### Chemoimmunotherapy enhances cellular metabolism in malignant cells and induces an immunosuppressive microenvironment in normal epithelial cells

Next, we investigated the population of epithelial cells. A total of 4963 epithelial cells were identified, and the cells were clustered into eight subclusters. The distributions of the cells and UMIs per spot were visualized via 2D t-SNE plots (Fig. 2A, Figure S4A), and the marker genes of each subcluster are shown in Fig. 4B. The fractions of the cells in each patient and group are shown in Fig. 4C, which revealed a significantly greater population of basal cells in the PT group (40% vs 80%, TN vs PT). The malignant cells and normal cells were distinguished via the inferCNV algorithm on the basis of copy number variations (CNVs) (Fig. 2D, Figure S4B, Table S5). We further investigated the distributions of epithelial cells in the aneuploid and diploid groups via traditional markers and found that basal cells accounted for 73% of aneuploid cells, whereas in diploid cells, basal cells (36%) and

(See figure on next page.)

**Fig. 2** Chemoimmunotherapy enhances cellular metabolism in malignant cells and induces an immunosuppressive microenvironment in normal epithelial cells. **A** t-SNE maps showing the distribution of epithelial cells in each sample and the distribution of different epithelial subtypes. **B** Heatmap showing the marker genes used for identification. **C** Bar plot showing the proportions of epithelial subtypes in each sample and group. LUAD: lung adenocarcinoma; LUSC: lung squamous cell carcinoma. **D** Clustering of the epithelial cells from all samples into aneuploid cells and diploid cells and t-SNE maps showing the distribution of epithelial cells in the TN and PT groups. **E** Bar plot (left) and heatmap (right) showing the fraction of each epithelial cell type in tumor cells and normal epithelial cells. **F** Volcano map showing the differentially expressed genes (DEGs) of tumor cells between TNs and PTs, and the top 10 DEGs are labeled. **G** Bar plot showing the significantly enriched pathways in malignant cells before and after chemoimmunotherapy. Bars in blue color indicate the enriched pathways after treatment, and bars in green indicate the enriched pathways before treatment. The pathways are ranked by GSVA score. Red arrows indicate the pathways selected for experimental validation. **H** Images from IHC staining for the clinical sample sections from five NSCLC patients. The detected proteins were labeled on the top of the panel, and the number of patients with treatment information /pathological assessment were labeled on the left of the panel. Scale bar = 30  $\mu$ m, magnificant = 400 X. **I, J** The spatial localizations of tumor cells, normal epithelial cells and other cell types were annotated in NSCLC sections via the RCTD algorithm, and the percentage of each cell type is shown in a bar plot. The tumor boundaries in tumor-3 were marked in yellow, and the boundaries of transition zone were marked in green. The areas of TLSs in tumor-2 were labeled by yellow dot lines. **K** Neighboring analysis of the spatial distance between all cell types. Within the white dotted line are pairs of cell types that show significant changes in spatial distance with increasing sensitivity to chemoimmunotherapy



normal epithelial cells were enriched in the “p53 signaling pathway”, “cell cycle”, “ECM–receptor interaction”, and “pyrimidine metabolism”. To study the changes in the biological functions of epithelial cells, we performed GSEA (Figure S4F, Figure S4G). The results revealed that in malignant cells, the functions enriched in the PT groups were related to cell metabolism, such as “drug metabolism”, “glutathione metabolism”, “tyrosine metabolism”, and “pyruvate metabolism”. In addition, “ferroptosis” and “protein digestion and absorption” were enhanced, suggesting that neoadjuvant treatment might induce ferroptosis and protein degradation and digestion in malignant cells. In addition, “EGFR tyrosine kinase inhibitor resistance” was weakened in the PT group, which may suggest that neoadjuvant treatment has the potential to increase the sensitivity of EGFR tyrosine kinase inhibitors (TKIs) in EGFR-TKI-resistant NSCLC patients. In normal epithelial cells, immune-related pathways, such as the “JAK-STAT signaling pathway”, “Toll-like receptor signaling pathway”, “IL-17 signaling pathway”, “Th1 and Th2 cell differentiation”, “cytokine–cytokine receptor interaction”, and “antigen processing and presentation”, were weakened in the PT group. In addition, some hallmark pathways, such as the “PI3K-Akt signaling pathway”, “mTOR signaling pathway”, and “Hippo signaling pathway”, were deactivated in the PT group. These findings indicate an exhausted and immunosuppressive microenvironment in normal epithelial cells after immunotherapy, and the activity of hallmark pathways, which may lead to the carcinogenesis of epithelial cells, is also inhibited.

To experimentally validate the alterations of hallmark pathways related to anti-tumor immunity and oncogenesis, we performed GSVA analysis to find the differential hallmark pathways in epithelial cells before and after chemoimmunotherapy. The most significant pathways were shown by a bar chart and ranked by GSVA score. Among them, we noticed that JAK/STAT3 pathway and IL2-STAT5 pathways were enhanced in PT group, while pathways closely related to tumor formation such as E2F pathway, TGF-beta pathway and WNT/Beta-catenin pathway were significantly inhibited in malignant cells after chemotherapy (Fig. 2G). IHC staining was performed in FFPE sections from the validation cohort, and results validated our findings from GSVA analysis, that chemoimmunotherapy enhanced the activity of pathways related to anti-tumor immunity and inhibited the hallmark pathways which are markers for tumorigenesis (Fig. 2H).

Next, we aimed to investigate the developmental trajectory of epithelial cells. Identifying the trajectory of malignant cells could reveal the key molecules and mechanisms that may drive the carcinogenesis of epithelial cells. The lineage trajectory for epithelial development

was inferred via Monocle 2 (Figure S3H). The trajectory begins with normal epithelial cells (diploid, state 2) and then progresses in two separate directions, with one direction leading to a carcinogenesis-like state but ending with normal cells (state 1), while the other direction eventually ending with malignant cells (state 3). Therefore, we believe that the trajectory from state 2 to state 3 simulates the development from normal epithelial cells to cancer cells. We next investigated the different branches of the development trajectory. Branch 1 started from state 2 and ended at state 1, and branch 2 started from state 2 and ended at state 3. In accordance with the observed alterations in gene expression, the genes were categorized into five distinct clusters (Figure S4I), and KEGG analysis was performed to identify the functions of the gene sets in each cluster. The genes in cluster 1, including the cancer biomarkers KRTs (KRT14, 17, and 19), TNF receptor genes (TNFRSF18 and TNFRSF1A), chemokine ligands (CXCL6, CXCL10, and CXCL14), and cell cycle regulators (CDK1, CDK4, CDKN1A, and CDKN2A), were significantly overexpressed in branch 2 but downregulated in branch 1. The genes in cluster 4, which included immunoglobulin proteins (IGHV1, IGHG1, and IGHV3), collagens (COL9A2, COL9A3, and COL2A1), fibroblast growth factors (FGF8, FGF17, and FGF18), and cell cycle regulators (CDK6, CCND1, and CCND2), were significantly overexpressed in state 1 but downregulated in state 3. The top 10 genes associated with the development of cell fate were shown in Figure S4J.

We investigated the cell compositions and spatial distributions in NSCLC tumors via data from spatial transcriptomic analysis (Fig. 2I, J). The RCTD algorithm was used to annotate the major cell types onto the paraffin sections. The populations of malignant cells reached over 80% in non-responders (tumor-1 and tumor-4) but were rarely observed in tumor-2. In tumor-3, the population of myeloid cells was the highest (30.69%). In addition, in tumor-2, the highest population of cells was fibroblasts. In addition, we observed the highest number of NK-T cells in the pCR group (tumor-2). Neighboring analysis was performed to assess the spatial distance between the major cell types (Fig. 2K). The results are shown from non-responders to pCR patients (from left to right). We found that the spatial distance from fibroblasts to tumor cells decreased as immunotherapy sensitivity increased, whereas the spatial distance to B cells gradually increased. In addition, the spatial distance between NK-T cells and B cells decreased. In addition, fibroblasts appeared to gradually colocalize with macrophages and NK-T cells at a distance, whereas this colocalization disappeared in pCR tissues because of a decrease in the proportion of fibroblasts.

### Immunotherapy inhibited the differentiation and function of Th17 CD4+ T cells and rescued CD4+ T cells from exhaustion

Lymphocytes play key roles in anticancer immunity. The colony expansion of T cells has been recognized as a key marker for predicting the response to immunotherapy. Therefore, we investigated CD4+ and CD8+ T cells via single-cell RNA and single-cell T cell receptor sequencing (scTCR-seq) to determine the dynamics of T cells in NSCLC patients after neoadjuvant therapy.

Eight distinct cell subtypes were identified by replastering 14,260 CD4+ T cells, including naïve, regulatory CD4+ T cells (Tregs), T helper 1 CD4+ T cells (Th1), T helper 17 CD4+ T cells (Th17), T follicular helper CD4+ T cells (Tfhs), T effector memory (Tem) CD4+ T cells, T resident memory (Trm) CD4+ T cells, and Trm-Foxp3+ CD4+ T cells (Fig. 3A). The distribution of CD4+ T cells in each sample and the UMIs in CD4+ T cells are shown by t-SNE plots (Figure S5A). The proportions of the CD4+ T-cell subtypes across different patients and groups were plotted (Figure S5B). To characterize the changes in CD4+ T-cell clonotypes after chemoimmunotherapy, the scTCR-seq data were analyzed to detect T-cell receptor (TCR) clonality and diversity. However, no significant differences were found in the expansion or diversity of CD4+ TCRs between TNs and PTs (Figure S5C to S5F). A comparison of the cell proportions between the TN and PT groups revealed a significant decrease in the number of Th17 cells, whereas the populations of Trm, Th1, and Tem cells tended to increase following neoadjuvant therapy (Fig. 3C). Th17 cells primarily secrete IL-17A, IL-17F, IL-21, IL-22, and CCL20 and have been identified as crucial regulators of

host immune responses against infection [31]. In human cancers, the Th17 lineage is known to perform both anti-tumor and carcinogenic functions [32, 33], and the Th17/Treg balance plays a pivotal role in antitumor immunity and autoimmunity [34]. In addition, high levels of IL-17A, which is mainly secreted by Th17 cells, increase resistance to PD-L1 blockade [35, 36]. Therefore, we believe that immunotherapy might block the differentiation of naïve CD4+ T cells into Th17 cells. Next, a KEGG analysis of genes upregulated in Th17 cells was performed to assess the biological functions of the cells (Fig. 3D). We found that the functions were enriched mainly in inflammation and infection diseases, such as COVID-19, Salmonella infection, shigellosis, and inflammatory bowel disease. Additionally, several hallmark pathways, such as the MAPK signaling pathway, the TGF-beta signaling pathway, and the FoxO signaling pathway, were also found to be associated with Th17 cells. The upregulated genes were also enriched in immune-related pathways such as cytokine-cytokine receptor interactions and the TNF signaling pathway, which is consistent with the findings that Th17 cells secrete cytokines such as IL-17A and activate the downstream pathway of TNF signaling. Next, we analyzed the exhaustion signature of CD4+ T cells by using exhaustion markers (LAG3, TIGIT, PCCD1, HAVCR2, CTLA4, LAYN, ENTPD1). Compared with those in the TN group, the exhausted signature of CD4+ T cells in the PT group was notably lower (Fig. 3E). When the subtypes were compared, Th17 and Trm cells presented the lowest exhaustion signature, whereas Tem cells presented the highest exhaustion signature (Fig. 3F, Figure S5G). The DEGs in each subtype between the TN and PT groups were analyzed, and the top 5 upregulated

(See figure on next page.)

**Fig. 3** Remodeling of CD4+ T cells after chemoimmunotherapy and the spatial distribution of CD4+ T-cell subclusters in NSCLC tumors. **A** Reclustering of CD4+ T cells into 8 subpopulations shown by a t-SNE plot (left) and the distribution of CD4+ T cells in the treatment-naïve and posttreatment groups (right). **B** Heatmaps showing the significantly upregulated genes in all the CD4+ T-cell subclusters. **C** Box plot showing the comparison of the fractions of CD4+ T-cell subtypes between the TN and PT (Wilcoxon, \* indicates  $P < 0.05$ ). **D** The top 20 KEGG pathways enriched with the upregulated genes in the CD4+Th17 subtype (adjusted  $P < 0.05$ ). **E** Violin plots comparing the average exhausted gene signature of CD4+ T cells between the TN and PT groups. The violin is bounded by the first and third quartile with a horizontal line at the median and whiskers extend to the maximum and minimum value.  $P$  values determined by two-sided Wilcoxon rank-sum test. **F** Violin plots comparing the average exhausted gene signature between CD4+ T-cell subtypes in the PT group.  $P$  values determined by two-sided Wilcoxon rank-sum test. **G** Bubble plot showing the top 20 KEGG pathways enriched by the DEGs from the CD4+Th17 subtype between the TN and PT groups. Each bubble indicates a signaling pathway (left), and the top 20 pathways associated with the relative bubbles are labeled, as listed in the right panel. Box plot indicating the proportion of Th17 CD4+ T cells (**H**), Treg CD4+ T cells (**I**) and ratio of Th17/Treg (**J**) in responder and non-responder.  $P$  values determined by Wilcoxon tests. **K** UMAP plot showing the cell subtypes identified in Hu's cohort. **L** UMAP plot showing the identification of subclusters of CD4+ T cells. UMAP plots demonstrating the expression of marker genes GZMA (**M**) and FOXP3 (**N**) in subclusters of CD4+ T cells. **O** The proportions of Th17 (left), Treg CD4+ T cells (middle) and ratio of Th17/Treg (right) in pre-treatment and post-treatment groups were shown by box plots.  $P$  values determined by Wilcoxon tests. **P** The proportions of Th17 (left), Treg CD4+ T cells (middle) and ratio of Th17/Treg (right) in non-responders and responders were shown by box plots.  $P$  values determined by Wilcoxon tests. **Q** Differentiation trajectory of all CD4+ T-cell subtypes; the subtypes are labeled with different colors. The numbers on the trajectory tree indicate the branch nodes, and the differentiation tree was divided into 5 branches. **R** Heatmaps showing the signature scores of Th17/Treg in each spot of the tissue sections. The spots were labeled with colors, and red color indicates high score, while blue color indicates low score. **S** Box plots showing the level of Log<sub>2</sub>(Th17/Treg) in each section (left) and each group (right). Each spot is considered as a duplicate, and  $P$  values were determined by two-sided Wilcoxon rank-sum test

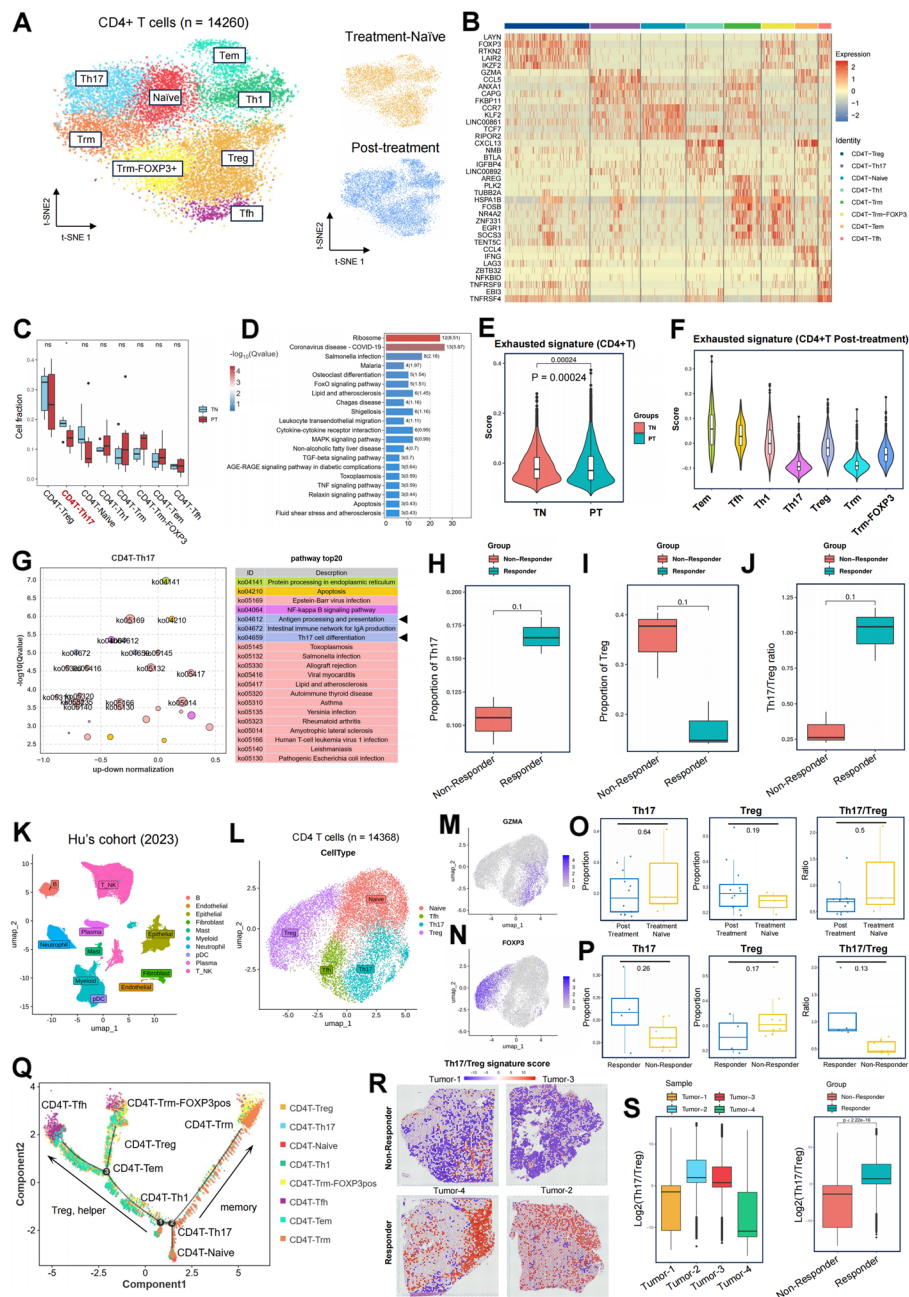


**Fig. 3** (See legend on previous page.)

genes in CD4+ T cells after combined therapy were identified (Figure S5H, Table S7). KEGG analysis and GSEA were performed on the DEGs of Th17 cells to analyze the alterations in the cellular functions of Th17 cells in response to immunotherapy (Fig. 3G, Figure S5I). Analysis of the top 20 enriched pathways by KEGG revealed that cellular functions such as the NF-kappa B signaling pathway (ko04064), antigen processing and presentation (ko04612), and Th17 cell differentiation (ko04659) were

inhibited after immunotherapy, which further confirmed that the fraction of Th17 cells was significantly reduced in PT patients. “Apoptosis” (ko04210) and “protein processing in the endoplasmic reticulum” (ko04210) were increased, suggesting that neoadjuvant therapy not only inhibited the differentiation but also induced the apoptosis of Th17 cells. GSEA also revealed significant inhibition of cellular functions related to infection, the immune response and carcinogenesis, such as the “B-cell receptor

signaling pathway”, “natural killer cell-mediated cytotoxicity”, “Yersinia infection”, “PI3K-Akt signaling pathway”, and “proteoglycans in cancer”.

In order to further investigate the correlation between alterations in Th17 and Treg cells and the sensitivity of chemo-immunotherapy, the proportions of Th17 cells and Treg cells were analyzed in responders (MPR and pCR patients) and non-responders (NMPR patients). The results demonstrated that, in responders, the distribution of Th17 cells was elevated (Fig. 3H) while the percentage of Treg cells showed a decreasing tendency (Fig. 3I). Furthermore, the ratio of Th17 and Treg cells showed an elevation (Fig. 3J), although this result did not reach statistical significance. To validate this finding, we downloaded single-cell transcriptomic data from a study by Hu et al. [20]. In Hu’s cohort, 3 pre-treatment and 12 post-treatment NSCLC patients (8 NMPR patients, 3 MPR patients and 1 pCR patient) were enrolled. The cell clusters were identified using the same marker genes, and the distribution of cell clusters was shown by UMAP plot (Fig. 3K), with 14,368 CD4+ T cells identified (Figure S5J, Fig. 3L). The expression of marker genes GZMA (Th17) and FOXP3 (Treg) were color-coded and indicated by UMAP plots (Fig. 3M, N). In accordance with the findings of this study, the proportion of Th17 cells and the ratio of Th17/Treg cells exhibited a downward trend in patients who had undergone post-treatment (Fig. 3O). Furthermore, the proportion of Th17 cells and the ratio of Th17/Treg cells increased following chemo-immunotherapy, while the proportion of Treg cells decreased after neoadjuvant therapy (Fig. 3P). The results from

Hu’s cohort further confirmed our findings that the distribution of Th17 cells within the TME and a markedly elevated Th17/Treg ratio can predict a favorable responsiveness to immunotherapy.

To clarify the differentiation pathways of CD4+ T cells and the characteristic genes associated with the differentiation states, we next reconstructed the proposed temporal differentiation trajectories of CD4+ T cells via Monocle 2 (Fig. 3Q, Figure S5K). In addition, RNA velocity was employed to construct a dynamic model of cell differentiation (Figure S5L). The reconstruction by Monocle 2 identified seven different developmental hierarchies (states 1–7), with cells differentiating from naïve cells and showing two major branches of differentiation (states 3 and 6). Additionally, two different developmental trajectories of further differentiation were identified, one of which commenced from state 3 (state 1 and state 2). Trm cells are located at the end of state 6, and Treg cells are located at the end of state 3. From state 3 onward, the cells exhibited two distinct branches of differentiation, subsequently differentiating into two populations of Tfh (state 1) and Trm-Foxp3+ cells (state 2) (Figure S5M). To elucidate the function of characteristic genes in the process of cell differentiation, we conducted an analysis of genes that exhibited significant alterations in conjunction with disparate cell differentiation paths. Our investigation focused on genes that underwent modification along two principal branches: one from state 5 to state 1 (Tfh cells located at the end of the branch), and the other from state 5 to state 6 (Trm cells located at the end of the branch). As shown in Figure S5N, the

(See figure on next page.)

**Fig. 4** Reshaping of CD8+ T-cell subclusters in NSCLC tissues by chemoimmunotherapy. **A** CD8+ T cells were reclustered into 8 subtypes, as shown by the t-SNE plot (left), and the distribution of CD8+ T cells in the TN and PT groups, as shown by the t-SNE plot (right). **B** Heatmap showing the significantly upregulated genes in each CD8+ T-cell subtype. **C** Box plot showing the comparison of the fractions of CD8+ T-cell subtypes between the TN and PT (Wilcoxon, \*\* indicates  $P < 0.01$ ). **D** Violin plots comparing the average exhausted gene signature of CD8+ T cells between the TN and PT groups. The violin is bounded by the first and third quartile with a horizontal line at the median and whiskers extend to the maximum and minimum value.  $P$  values determined by two-sided Wilcoxon rank-sum test. **E** Violin plots comparing the average cytotoxic gene signatures of CD8+ T cells between the TN and PT groups ( $P$  values from two-sided Wilcoxon rank-sum test). **F** Violin plots comparing the exhausted gene signature between CD8+ T-cell subtypes in the PT group. **G** Violin plots comparing the cytotoxic gene signatures of CD8+ T-cell subtypes in the PT group. **H** The top 20 KEGG pathways enriched with the upregulated genes in the CD8+ Teff KLRG-high subgroup (adjusted  $P < 0.05$ ). **I** Top 10 upregulated or downregulated KEGG pathways enriched with the DEGs in the CD8+ Teff KLRG-high subgroup between the TN and PT groups (adjusted  $P < 0.05$ ). **J** The top 20 KEGG pathways enriched with the upregulated genes in the CD8+ Teff ZNF683-high subtype (adjusted  $P < 0.05$ ). **K** Top 10 upregulated or downregulated KEGG pathways enriched by the DEGs in the CD8+ Teff ZNF683-high subtype between the TN and PT groups (adjusted  $P < 0.05$ ). **L** The developmental trajectory of CD4+ T cells from all samples colored according to pseudotime; the color from light to dark indicates the progression of pseudotime. **M** The developmental trajectory of CD8+ T cells colored according to their differentiation state. **N** Differential trajectory of all CD8+ T-cell subtypes; the subtypes are labeled with different colors. The numbers on the trajectory tree indicate the branch nodes, and the differentiation tree was divided into 3 branches. **O, P** The developmental trajectory of CD8+ T cells in the TN group and PT groups. **Q** Pseudo-heatmap showing the significant genes correlated with the differentiation of CD8+ T cells from state 2 to state 4 (from naïve to regulator) and state 2 to state 1 (from naïve to memory). The genes were subjected to 5 clusters, and the top 50 genes correlated with pseudotime are shown, with the selected KEGG pathways enriched in each gene cluster labeled on the left. **R** Spatial distributions of CD4+ and CD8+ T cells in 4 NSCLC sections according to the RCTD algorithm; each color indicates a distinct cell type. **S** Violin plot showing the proportion of CD8+ T cells in each section. Each spot is considered as a duplicate, and  $P$  values were determined by two-sided Wilcoxon rank-sum test, \*\*\*\* indicates  $P < 0.0001$ , Wilcoxon test

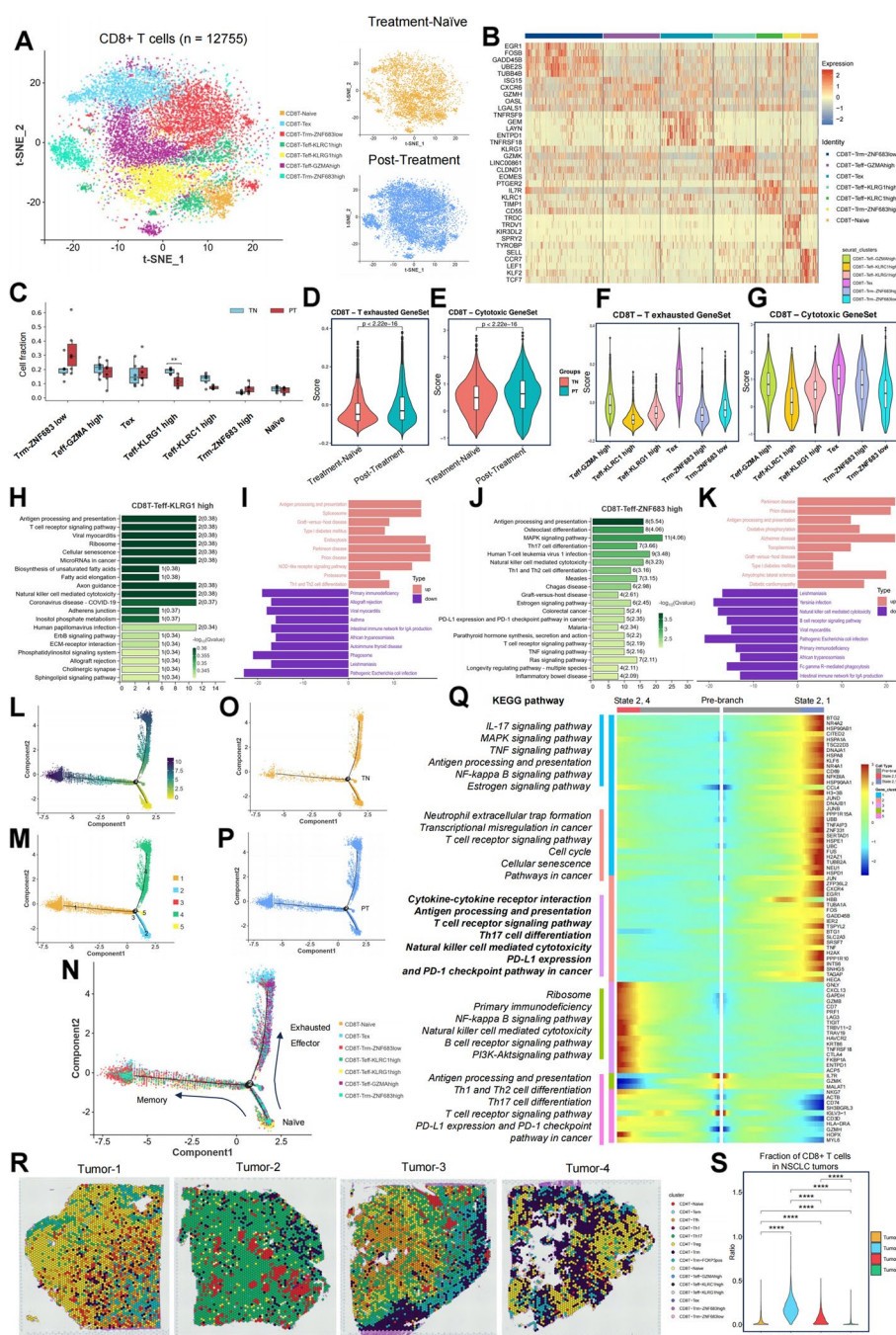


**Fig. 4** (See legend on previous page.)

genes were classified into 5 clusters on the basis of their expression trends, and KEGG analysis was performed to assess the biological functions of each gene cluster. The trends in gene expression exhibited two distinct directions. The first was a notable elevation in gene expression levels as the pseudotime progressed from state 5 to state 6 (clusters 1 and 4). The second was a similarly pronounced increase in gene expression levels as the

pseudotime time progressed from state 5 to state 1 (clusters 2, 3, and 5). We found that genes in cluster 1 were enriched in functions such as Th17 differentiation (FOS, HSP90AA1, NKFB1, NFKBIA, and STAT3), antigen processing and presentation (HLA-A), cytokine–cytokine receptor interaction (CXCR3), and the T-cell receptor signaling pathway. Intriguingly, genes in cluster 2 were enriched in pathways related to non-small cell lung

cancer (GADD45G, CDKN1A, PRKCA), transcription misregulation in cancer, and the estrogen signaling pathway (Figure S5O).

In order to further elucidate the spatial distribution of Th17 and Treg cells in NSCLC tumors, the RCTD algorithm was employed to annotate the coordinates of Th17 and Treg cells in four NSCLC sections, including two non-responders and two responders. Furthermore, the Th17/Treg ratio was scored in each spot of the sections to demonstrate the significance of the Th17/Treg ratio in assessing the sensitivity of immunotherapy. A significant high score of the Th17/Treg ratio was observed in responders, especially in the non-malignant regions (Fig. 3R). Statistical analysis demonstrated a significant high ratio of Th17/Treg and a high level of Th17 cells in responders (Fig. 3S, Figure S5P), and a high level of Treg cells in non-responders, thereby supporting our findings from the single-cell RNA sequencing analysis.

#### **Responders to chemoimmunotherapy exhibited significantly increased infiltration of effector CD8+T cells in NSCLC tumors**

A total of 12,755 CD8+T cells were identified via scRNA-seq and were clustered by canonical marker genes: naïve, exhausted, effector, and memory. The effectors were further clustered into 3 subpopulations by high expression of the marker genes KLRG1, KLRC1, and GZMA, while the memory cells were divided by the expression level of ZNF683 (Fig. 4A, B). The distribution of CD8+T cells in each sample and the UMIs in CD8+T cells are shown by t-SNE plots (Figure S6A). GZMA is a canonical cytotoxic marker, while CD8+T cells highly expressing KLRG1 are defined as short-lived effector cells but are also recognized as having a cytotoxic phenotype [37, 38]. KLRC1, also known as NKG2A, is an inhibitory receptor expressed in cytotoxic T cells and NK cells [39, 40]. The ligand of KLRC1 is the MHC I class HLA-E molecule [41], and the recognition of HLA-E by KLRC1 can lead to the immune evasion of HLA-E-positive tumor cells [42]. Therefore, KLRC1 has also been identified as an immune checkpoint molecule, and KLRC1 blockade was shown to work with ICBs to potentiate the immunity of CD8+T cells [42–44]. The proportions of CD8+T cells in each sample and group are shown in a bar plot (Figure S6B). When we compared the fraction of subclusters of CD8+T cells between TNs and PTs, we found a significant decrease in the number of effector-KLRG1 cells in the PT group (Fig. 4C). We also analyzed the exhausted and cytotoxic signatures of CD8+T cells between TNs and PTs, and the cytotoxic signature was evaluated via canonical cytotoxic markers (GZMA, GZMB, GZMK, GNLY, IFNG, PRF1, and NKG7). We found that neoadjuvant therapy significantly inhibited

the exhausted signature and enhanced the cytotoxic capacity of CD8+T cells (Fig. 4D, Fig. 4E). In addition, we compared the exhausted and cytotoxic signatures of each subtype (Fig. 4F, Figure S6C), and exhausted CD8+T cells presented the strongest exhaustion score, as expected. In addition, exhausted CD8+T cells also presented the highest cytotoxic score in the PT group, whereas in the TN group, exhausted, Trm ZNF683<sup>high</sup> and GZMA<sup>+</sup>effector high cells presented relatively high cytotoxic scores (Fig. 4G, Figure S6D). The DEGs in each subcluster between TNs and PTs were analyzed (Table S8), and the significantly upregulated genes in PTs are shown in a bubble plot (Figure S6E). With the help of scTCR-seq analysis, alterations in the TCR clonotypes of CD8+T cells were analyzed to investigate the expansion and diversity of TCRs after combined therapy. However, no significant differences were found between the TN and PT groups (Figure S6F to Figure S6I).

We then investigated the functions of Teff-KLRG1 in CD8+T cells, the number of which is inhibited by combined therapy. KEGG analysis was performed on the genes whose expression was upregulated in Teff-KLRG1 cells. The results revealed that the pathways enriched were “antigen presenting and presentation” (CD74, HLA-F), “T-cell receptor signaling pathway” (FYN, NKC2), and “natural killer cell-mediated cytotoxicity” (FYN, SH2D1A) (Fig. 4H). Teff-KLRG1 cells highly express CD44, which is commonly expressed in cancer stem cells and is related to cancer development and metastasis. CD27, which is involved in T-cell activation and B-cell immunity [45], is also highly expressed in Teff-KLRG1. KEGG and GSEA analyses were performed to measure alterations in Teff-KLRG1 cell functions after combined therapy, and the results revealed that “antigen presenting and presentation” was significantly enhanced in PTs; however, immune-related pathways such as the “B-cell receptor signaling pathway”, “natural killer cell-mediated cytotoxicity”, the “NF-kappa B signaling pathway”, “neutrophil extracellular trap formation”, and “primary immunodeficiency” were inhibited after combined therapy. In addition, some hallmark pathways, such as the “PI3K-Akt signaling pathway”, “Hippo signaling pathway”, “small cell lung cancer”, and “WNT signaling pathway”, were also inhibited in PTs. These findings indicate a controversial role of Teff-KLRG1 cells in the TME (Fig. 4I, Figure S6J). ZNF683-high CD8+T cells are associated with antitumor immunity following PD-1 blockade [46], and we also assessed the function of Teff-ZNF683-high T cells by analyzing the upregulated genes. Teff-ZNF683 cells highly expressed T-cell receptors (TRAC, TRBC1), killer cell lectin-like receptor subfamily genes (KLRD1, KLRK1), PIK3R1, FOS, and MAPK1, and the upregulated genes were enriched in the “antigen

processing and presentation”, “MAPK signaling”, “natural killer cell-mediated cytotoxic”, “PD-L1 expression and PD-1 checkpoint pathway in cancer”, and “T-cell receptor signaling pathway” pathways (Fig. 4J). KEGG analysis was also performed to evaluate the functional enrichment of the DEGs in Teff-ZNF683 cells, and the results revealed the top 10 upregulated and downregulated pathways. The “antigen processing and presentation” pathway was enhanced, whereas the “natural killer cell-mediated cytotoxic” and “B-cell receptor signaling pathway” pathways were inhibited after PD-1 blockade (Fig. 4K). These findings indicated that Teff-ZNF683 cells switched to an inactivated and antigen-presenting phenotype after immunotherapy.

To investigate the differentiation paths of CD8+T cells, the RNA velocity was used to construct a dynamic model of cell differentiation (Figure S6K). Next, we used Monocle 2 and Slingshot to perform the cell developmental trajectory analysis. Monocle 2 identified 5 states and two major branches, which started from naïve cells, and the exhausted cells were located at the ends of both branches (Fig. 4L, M). From the branch node, the cell trajectory went in two different directions: one direction was differentiation to effector cells, mainly GZMA high effectors, and the other path direction was to memory cells, including Trm-ZNF683 high and ZNF683low cells (Fig. 4N, Figure S6L to S6O). The differentiation trajectory of TNs and PTs suggested a significant improvement in the progression of cell development following neoadjuvant therapy (Fig. 4O, P). Slingshot revealed three different lineages of CD8+T cells (Figure S6P): lineage 1 is from Naïve, goes through Teff-KLR1 and Trm-ZNF683 low, and ends at exhausted; lineage 2 starts from Naïve and goes through Teff-KLRG1 high, Teff-GZMA high and ends at exhausted; lineage 3 starts from Naïve and goes through Teff-KLR1, Trm-ZNF683 low and ends at Trm-ZNF683 high. The cell trajectory identified by Slingshot supported the differentiation model identified by monocle 2. Having established the cell trajectory of CD8+T cells, we then investigated the genes correlated with cell development. The genes were grouped into 5 clusters according to their expression trends, and the top 10 genes in each cluster are shown by a heatmap (Figure S6Q). The genes within the gene set cluster 2, whose expression increased with increasing pseudotime, presented a pattern of change that was consistent with the differentiation of CD8+T cells. The genes in cluster 2 were enriched in pathways related to TCR signaling, NF- $\kappa$ B signaling, TNF signaling, HIF-1 signaling, TGF- $\beta$  signaling, the cell cycle, and P53 signaling. Next, we analyzed the genes correlated with different developmental fates of CD8+T cells. There are two major branches of the trajectory: branch 1 ends at the state of exhausted

and memory T cells (states 2 to 1), whereas branch 2 ends at the state of exhausted and effector T cells (states 2 to 4). We identified 1764 genes that correlated with the two major developmental branches, and the top 60 genes are shown in Fig. 4Q. Notably, with respect to cell fate from naïve cells to effectors, upregulated genes were enriched in “cytokine–cytokine receptor interaction”, “T-cell receptor signaling pathway”, “Th17 cell differentiation”, “natural killer cell-mediated cytotoxicity”, and “PD-L1 expression and the PD-1 checkpoint pathway in cancer”, suggesting that the CD8+T cells developed a cytotoxic and activated phenotype.

Next, we studied the spatial distribution of CD8+T-cell subtypes, and neighboring analysis was subsequently performed to assess the spatial distance between CD8+T-cell subtypes and other major cell types, including cancer cells, B-plasma cells, CAFs, and macrophages (Figure S6R). However, the results revealed no positive neighboring relationships between CD8+T cells and the other cell types. The RCTD algorithm was employed to annotate the coordinates of CD4+T cells and CD8+T cells in the section slides to visualize the distribution of T lymphocytes in the four NSCLC sections (Fig. 4R). The proportions of CD8+T cells and CD8+effector cells in each section were subsequently calculated, and the results revealed significant enrichment of CD8+T cells and CD8+effector cells in tumor-2 (pCR) tumors, followed by tumor-3 (responder) tumors (Fig. 4S, Figure S6S). The sections were then subgrouped into responders (tumor-2 and tumor-3) and non-responders (tumor-1 and tumor-4), and not surprisingly, the fractions of CD8+T cells and CD8+effectors were significantly elevated in the responders (Figure S6T, Figure S6U). These results from four NSCLC tumor sections suggested that the infiltration level of CD8+T cells was correlated with the responsiveness to chemoimmunotherapy in NSCLC patients.

#### **Anti-PD-L1 therapy increased the infiltration of IgG+ plasma cells and enhanced the communication between plasma cells and CAFs/macrophages**

Tumor-infiltrating B cells are important components of the TME, and the activation of TIBs has been shown to be involved in the immune checkpoint inhibitor response in NSCLC. To further clarify the effects of chemoimmunotherapy on B-cell differentiation and activation, we identified a total of 12,823 B cells via scRNA-seq and recustered them into 5 subpopulations, including naïve B cells (TCL1A, IL4R, CD200, YBX3, FCER2), germinal center B cells (MYBL1, RGS13, SUGCT, MEF2B, SERPINA9), plasma cells (IGHV3–29, IGHV2–5, IGKV1–39, IGKV1–17, IGLV1–47), memory B cells (NR4A2, DNAJA1, NR4A1, CD83, DUSP2) and follicular B

cells (TMPO, ARHGEF18, H1–4, ALOX5, RALGPS2) (Fig. 5A, Figure S8A to S8D). The immunoglobulin (Ig) isotypes were inferred via single-cell B cell receptor sequencing (scBCR-seq), and 4 antibody isotypes were detected, namely, IgA, IgG, IgD, and IgM (Fig. 5B). In addition, the antibody isotypes in each B-cell subcluster were analyzed via scBCR-seq. The naïve B-cell cluster was dominated by the IgM isotype, the germinal center B cell (GCB) and plasma cell clusters presented high enrichment of the IgG isotype, and the memory B-cell and follicular B-cell subtypes presented different isotypes (Fig. 5C). The percentages of B-cell subclusters in each sample and subgroup were also analyzed, and the results suggested a significant decrease in the plasma cell subtype after combined therapy, whereas the memory B-cell subtype tended to increase in the PT group (Fig. 5D, E). The ratios of antibody isotypes between subtypes were also compared, which revealed that the enrichment of the IgG isotype decreased after therapy, which was consistent with the dynamics of plasma B cells, as IgG is the dominant antibody isotype in plasma cells (Fig. 5F). The DEGs in B-cell subclusters between TNs and PTs were analyzed, and the top 5 upregulated genes in the PT group were identified (Figure S8E, Table S9). ScBCR-seq was also performed to evaluate the colony diversity and expansion of B cells; however, no positive findings were detected in B cells between the TN and PT groups (Figure S8F to S8I).

Next, we aimed to perform an in-depth analysis of the differentiation of B cells. We first constructed the differentiation trajectory of B cells via Monocle 2, and the results revealed that cellular differentiation started with naïve B cells and progressed in two different branching

directions, ending with memory B cells and plasma B cells, respectively, and three different cellular differentiation states were obtained (Fig. 5G). Monocle 3 yielded a more complex cellular differentiation trajectory but broadly supported the results of Monocle 2, suggesting that cells differentiated from naïve B cells in two distinct directions, i.e., toward plasma cells and memory B cells, and that follicular B cells are basically located at the intersection of the branches involved in cellular differentiation (Fig. 5H, I). The cell differentiation trajectory map constructed by monocle 3 revealed the differentiation positions of the TIBs subpopulations over pseudotime, with the majority of memory B cells and a small proportion of plasma cells at the end of the pseudotemporal trajectory, whereas CytoTRACE analyses revealed that plasma cells presented a greater degree of cell differentiation (Fig. 5J).

Having constructed the cell differentiation trajectory, we first analyzed the genes that exhibited dynamic changes with the progression of pseudotime (Figure S8J). The genes were grouped into 3 clusters according to their dynamic changes in expression. The cell cycle and DNA damage regulators CDKN1A and CKS2 and the activation marker for antigen-presenting CD83 cells were highly expressed at the root of the pseudotemporal trajectory, and the MHC-related genes HLA-B and HLA-DOB and the immunoglobulin genes, mainly the IGKV cluster, were highly expressed in the middle of the trajectory. We further investigated the genes correlated with two major developmental branches of B cells (Fig. 5K). Branch 1 is from state 3 to state 1, and memory B cells are located at the end of the path. Branch 2 spans from state 3 to state 2, indicating that the cell differentiated from naïve B cells to plasma cells. The genes associated with

(See figure on next page.)

**Fig. 5** In response to anti-PD-L1 therapy, increased infiltration of IgG+ plasma cells and enhanced communication between plasma cells and CAFs/macrophages were detected. **A** Reclustering of B cells into 5 subpopulations shown in the UMAP plot, colored by subtype. **B** UMAP showing the distribution of antibody isotypes identified by scBCR-seq, colored according to different antibody isotypes. **C** Bar plot showing the percentages of different antibody isotypes in B-cell subtypes. **D** The percentages of B-cell subtypes in each sample and group. **E** Box plot showing the comparison of the fractions of CD4+ T-cell subtypes between the TN and PT (Wilcoxon, \* indicates  $P < 0.05$ ). **F** Box plot showing the comparison of the percentages of antibody isotypes between TNs and PTs (Wilcoxon, \* indicates  $P < 0.05$ ). **G** The developmental trajectory of B cells from all samples colored with pseudotime; the color from light to dark indicates the progression of pseudotime (upper). The differentiation trajectories of B-cell subtypes (middle) and differentiation states (lower) are labeled with different colors. The numbers on the trajectory tree indicate the branch nodes, and the differentiation tree was divided into 2 branches. **H** t-SNE plot showing the B cells colored according to pseudotime, inferred by monocle 3. **I** t-SNE map showing the distribution of B cells of different subtypes inferred via monocle 3. **J** UMAP plot showing the differentiation of B cells according to pseudotime (left) or the CytoTRACE score (right), inferred by monocle 3 or CytoTRACE. The memory B cells and plasma B cells are labeled with black dotted lines. **K** Pseudo-heatmap showing the significant genes correlated with the differentiation of B cells from stage 3 to stage 1 (from naïve to memory) and from stage 3 to stage 2 (from naïve to plasma). The genes were subjected to 5 clusters, and the top 10 genes correlated with pseudotime in each cluster are shown, with the selected KEGG pathways enriched in each gene cluster labeled on the left. **L** Spatial annotation of B-cell subtypes, tumor cells, macrophages, T cells, Endos, and CAFs in 4 NSCLC tumor sections inferred via the RCTD algorithm. The white dotted lines indicate the TLS region, and the TLS regions were labeled TLS-1 to TLS-4. **M** Heatmap showing the neighboring relationships between B-cell subtypes and tumor cells, macrophages, T cells, Endos, and CAFs in each NSCLC section. The white dotted line represents the pair of plasma B-CAFs, which shows significant changes in spatial distance with increasing sensitivity to chemoimmunotherapy. The number on the bar indicates the number of cells that have neighboring relationships

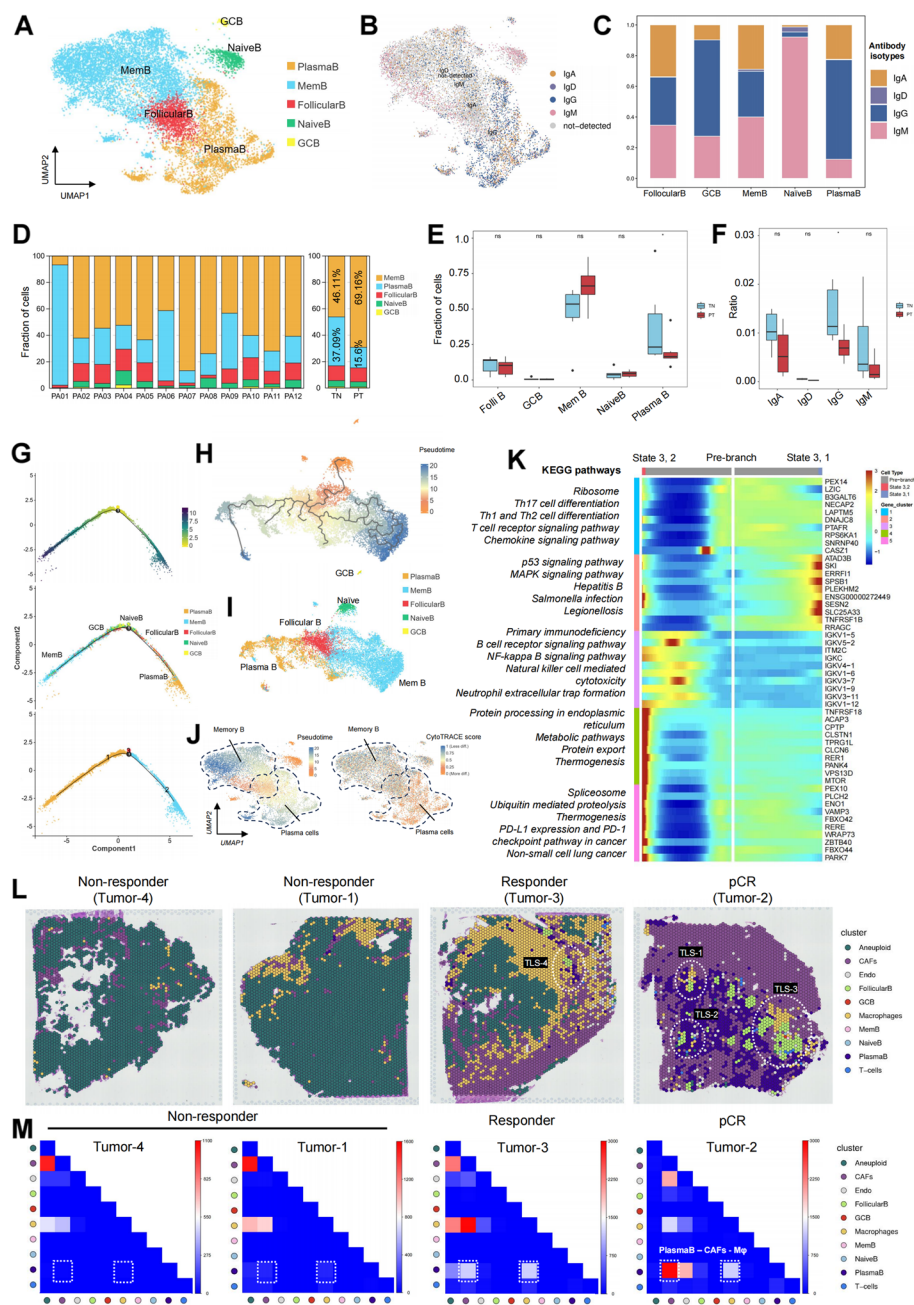


**Fig. 5** (See legend on previous page.)

cell differentiation were grouped into 5 clusters according to the dynamic changes in gene expression. The cluster 2 genes, including the NF- $\kappa$ B signaling genes NFKB1 and RELB and chemokines and chemokine receptors such as CXCL8, CCL3, and CXCR5, were highly expressed at the end of branch 1. The cluster 3 genes were correlated with the developmental trajectory of plasma B cells, and KEGG analysis suggested that the genes were significantly enriched in the BCR signaling, NF- $\kappa$ B signaling,

natural killer cell-mediated cytotoxicity, and neutrophil extracellular trap formation pathways, indicating an activated phenotype of B cells. In addition, cluster 5 genes, which were highly expressed at the end of the trajectory of plasma cells, were enriched in the pathways “non-small cell lung cancer” (GADD45A, GADD45B, KRAS, PIK3CA, PIK3CB, and FOXO3) and “PD-L1 expression and PD-1 checkpoint pathway in cancer” (EGFR, FOS,

JUN, and HIF1A). The overexpression of oncogenes might enhance tumor proliferation and immune evasion.

To analyze the spatial distribution and proximity of B cells to other major cell types in NSCLC tissue sections, we performed spatial annotation and neighboring analysis of B-cell subpopulations, as well as malignant epithelial cells, macrophages, CAFs, and T cells, in 4 NSCLC tissue sections via the RCTD algorithm. The infiltration of plasma cells and follicular B cells was markedly elevated in pCR (tumor-2) and responder (tumor-3) tissues, whereas it was nearly undetectable in nonresponder tissues (tumor-1 and tumor-4) (Fig. 5L). This finding is consistent with the reported results that high infiltration of B cells predicts better responsiveness to immune blockade therapy [47–49]. In addition, we detected a high proportion of follicular B cells within the TLS structures. In TLS-3, a high diversity of B cells, including naïve B cells, GCBs, plasma B cells, and follicular B cells, was observed. Neighboring analysis suggested that plasma cells notably colocalized with CAFs and macrophages in the tumor tissues of responders but not in those of non-responders. We analyzed the antibody isotypes in the four NSCLC sections and found that only the IgG isotype showed the highest intensity in the pCR section (tumor-2) (Figure S8K). Next, we further analyzed the intensity of the antibody isotypes in the pCR section and found that the intensity of IgM isotype significantly overlapped with that of the TLS structures, whereas that of IgG isotype overlapped with that of plasma cells (Figure S8L), which suggests that plasma cells of the IgG isotype show significant tissue infiltration with increased sensitivity to ICB therapy, whereas B cells in the TLSs are predominantly of the IgM isotype. Neighboring analysis demonstrated notable colocalization between plasma cells (mainly IgG + plasma cells) and CAFs/macrophages in responders, indicating that the infiltration of IgG + plasma cells and neighboring relationships with CAFs and macrophages might suggest a positive response to anti-PD-L1 therapy (Fig. 5M). In contrast, evidence suggests that the co-occurrence of IgA plasma cells and CAFs/macrophages in lung adenocarcinoma supports an immunosuppressive TME [50]. In addition, the occurrence of follicular B cells (mainly the IgM isotype) was found to be associated with the formation of TLSs, and were localized in the center of TLS regions.

Since we found that plasma cells colocalized with CAFs/macrophages in positive responders to chemoimmunotherapy, we then performed a cell–cell interaction analysis to investigate alterations in cell communication patterns after chemoimmunotherapy by using CellChat. The relative pathways related to the information flow between the cell types in TNs and PTs are shown in a bar plot (Figure S8M, Table S10), which demonstrated that

pathways such as MHC-II, GAS, and SPP1 were significantly enriched before therapy; however, the communication pathways of IL-16, MHC-I, CXCL, and MIF were notably enhanced after therapy (Figure S8N). In addition, pathways including the IGF, CSE, and VCAM pathways were distinct in the PT group, suggesting newly established communication patterns between the cell types.

#### **Chemoimmunotherapy notably changed the proportions of CXCL9 and SPP1 macrophages and enhanced the infiltration of TAMs in the NSCLC TME**

To investigate the heterogeneity of myeloid cells extensively, 5725 myeloid cells were clustered into 11 subpopulations, among which 8 subtypes were Mφs, 2 were dendritic cells (DCs), and 1 was a monocyte cell subtype (mono-CX3CR1) (Fig. 6A, Figure S9A, Figure S9B, and Figure S9C). The fractions of the cell subpopulations in each sample and group were analyzed (Figure S9D). Among the myeloid cells, we focused on the heterogeneity and functions of Mφ subpopulations in the TME, as the crucial role of Mφ in the inflammatory response and antitumor immunity has been firmly established; additionally, Mφ constitute the majority of myeloid cells in our data. The classical marker gene was used to categorize Mφs into 8 distinct subpopulations: Macro-ISG15, Macro-SELENOP, Macro-CXCL9, Macro-CXCL2, Macro-SPP1, Macro-MCEMP1, and Macro-proliferating. The macro-MCEMP1 subtype comprises tissue-resident alveolar macrophages (AMs), as it highly expresses canonical AM markers (MCEMP1 and MARCO). In contrast, other Mφ subtypes were identified as tumor-associated macrophages (TAMs). Mφ-SPP1 has been reported to be involved in tumor angiogenesis and immune escape [51, 52]. Our findings revealed that Mφ-SPP1 cells highly expressed numerous oncogenes, including GRB2, ENO1 and SLC3A2. Additionally, KEGG analysis indicated that this subcluster may be involved in oncogenic signaling pathways, such as the mTOR signaling pathway, the HIF-1 signaling pathway and the ferroptosis pathway. Mφ-SELENOP reportedly has anti-inflammatory functions [53]. Mφ-CXCL9 highly expresses proinflammatory chemokines such as CXCL9 and CXCL10, which attract T cells and NK cells through their antigen-presenting capacity. Mφ-ISG15 highly expresses the interferon-responsive factor ISG15, suggesting that it may act as a proinflammatory and antigen-presenting agent by activating the interferon signaling pathway. Mφ-CXCL2 cells play a role in the induction of neutrophil aggregation via the CXCL2-CXCR2 pathway [54, 55]. Furthermore, CXCL2 is involved in the crosstalk between macrophages and other immune cells, as well as between macrophages and tumor cells [56]. Mφ-proliferating cells are known

to highly express genes related to the cell cycle and DNA replication, such as MKI67 and CDKN3.

To further elucidate the function of macrophage subtypes and the impact of combination therapy on macrophage function and polarization trends, we conducted a comprehensive analysis of the M1 and M2 phenotypes, angiogenesis signatures, and phagocytosis signatures (Fig. 6B, Table S11) of the macrophages as a whole [57], as well as of individual subpopulations. Additionally, we examined the alterations in these functions between the TN and PT groups. We found that the M1 signature of macrophages was significantly elevated in the PT group, whereas the M2 signature was significantly decreased in the PT group. In addition, both the angiogenesis and phagocytosis signatures of macrophages were significantly decreased in the PT group. The functions of individual macrophage subpopulations were analyzed, and the phagocytosis signatures of M $\phi$ -SELENOP and M $\phi$ -ISG15 were significantly greater than those of the other subpopulations (Figure S9E, Figure S9F). Furthermore, almost all the TAMs, with the exception of M $\phi$ -CXCL9, presented higher M2 signatures, particularly M $\phi$ -SPP1, M $\phi$ -SELENOP and M $\phi$ -ISG15. The results of the aforementioned analysis demonstrated that M $\phi$ -SPP1, M $\phi$ -SELENOP and M $\phi$ -ISG15 exhibited a more pronounced trend toward M2 polarization and are likely to be involved in tumor progression and metastasis as pro-oncogenic factors. Furthermore, CXCL9 macrophages display cytokine secretion characteristics that may be involved in antigen presentation, as well as anti-inflammatory or antitumor immunity. More importantly, we examined the difference in the fractions of myeloid cells between the TN and PT groups and discovered

that the proportion of M $\phi$ -CXCL9 cells was markedly elevated in the PT group (Fig. 6C), substantiating the hypothesis that combination therapy markedly enhances the antigen-presenting and immune-activating functions of macrophages in the TME. KEGG analysis revealed that CXCL9 macrophages highly expressed chemokines, proinflammatory factors and MHC genes and were involved in immune-related signaling pathways such as the “chemokine signaling pathway”, “antigen processing and presentation”, “TNF signaling pathway”, and “IL-17 signaling pathway” (Fig. 6D). Furthermore, DEGs of each cell subpopulation between TNs and PTs were analyzed (Figure S9G, Table S12), and KEGG analysis of the DEGs in M $\phi$ -CXCL9 between TNs and PTs suggested that most cellular functions, including “antigen processing and presentation”, “IL-17 signaling pathway”, “TNF signaling pathway”, and “toll-like receptor signaling pathway” (Fig. 6E), were enhanced, indicating that the characteristic functions of M $\phi$ -CXCL9 macrophages were further activated after chemoimmunotherapy.

To provide further clarification regarding the differentiation trajectories of the macrophage subpopulations, we employed Monocle 2 software to construct a tree of macrophage differentiation (Fig. 6F, G). Our analysis indicated that the cellular differentiation trajectory started with M $\phi$ -MCEMP1 and subsequently exhibited two principal differentiation branches, with M $\phi$ -SPP1 in the beginning, M $\phi$ -ISG15 and M $\phi$ -proliferating near the first branch point, ending with M $\phi$ -CXCL9 and M $\phi$ -CXCL2, and M $\phi$ -SELENOP, respectively (Fig. 6H). In addition, developmental trajectory analysis revealed five different cell differentiation states. The cell differentiation trajectories were

(See figure on next page.)

**Fig. 6** Chemoimmunotherapy notably changed the proportions of CXCL9 and SPP1 macrophages and enhanced the infiltration of TAMs in the NSCLC TME. **A** Reclustering of myeloid cells into 11 subpopulations, as shown by the t-SNE plot. **B** Violin plots comparing the M1 signature, M2 signature, angiogenesis signature, and phagocytosis signature of all macrophages between the TN and PT groups ( $P$  values from Wilcoxon tests). **C** Box plot showing the comparison of the fractions of macrophage subtypes between TNs and PTs (Wilcoxon, \* indicates  $P < 0.05$ , \*\* indicates  $P < 0.01$ ). **D** The top 20 KEGG pathways enriched with the upregulated genes in the CXCL9+ macrophage subtype (adjusted  $P < 0.05$ ). **E** Bubble plot showing the top 20 KEGG pathways enriched with the DEGs from the CXCL9+ macrophage subtype between the TN and PT groups. Each bubble indicates a signaling pathway (left), and the top 20 pathways associated with the relative bubbles are labeled, as listed in the right panel. **F** The developmental trajectory of the macrophages from all the samples colored according to pseudotime; the color from light to dark indicates the progression of pseudotime. **G** The developmental trajectory of B cells according to their differentiation state. **H** The differentiation trajectory of all the macrophage subtypes; the subtypes are labeled with different colors. The numbers on the trajectory tree indicate the branch nodes, and the differentiation tree was divided into 4 branches. **J** The pseudo-heatmap showing the significant genes correlated with the differentiation of macrophages. The genes were subjected to 5 clusters, and the top 10 significant genes are shown. **I** Spatial annotation of macrophage subtypes, tumor cells, NK cells, T cells, and CAFs in 4 NSCLC tumor sections inferred via the RCTD algorithm. **J** The percentages of indicated cell types in 4 NSCLC tumor sections were calculated and shown by bar plot. **K** Violin plots showing the proportions of SPP1 (left), CXCL9 (middle) and SELENOP (right) macrophages in non-responders and responders. Each spot is considered as a duplicate, and  $P$  values were determined by two-sided Wilcoxon rank-sum test. **L** Heatmap showing the neighboring relationships between macrophage subtypes and tumor cells, NK cells, T cells, and CAFs in each NSCLC section. The pairs of cells that show significant changes in spatial distance with increasing sensitivity to chemoimmunotherapy are within the white dotted line. The number on the bar indicates the number of cells that have neighboring relationships. Multiple immunofluorescence (mIHC) staining of the macrophage subpopulations, SPP1 and CXCL9, and tumor cells in NSCLC tissue sections from the TN (**M**) and PT (**N**) groups. The scale bar represents 100  $\mu$ M

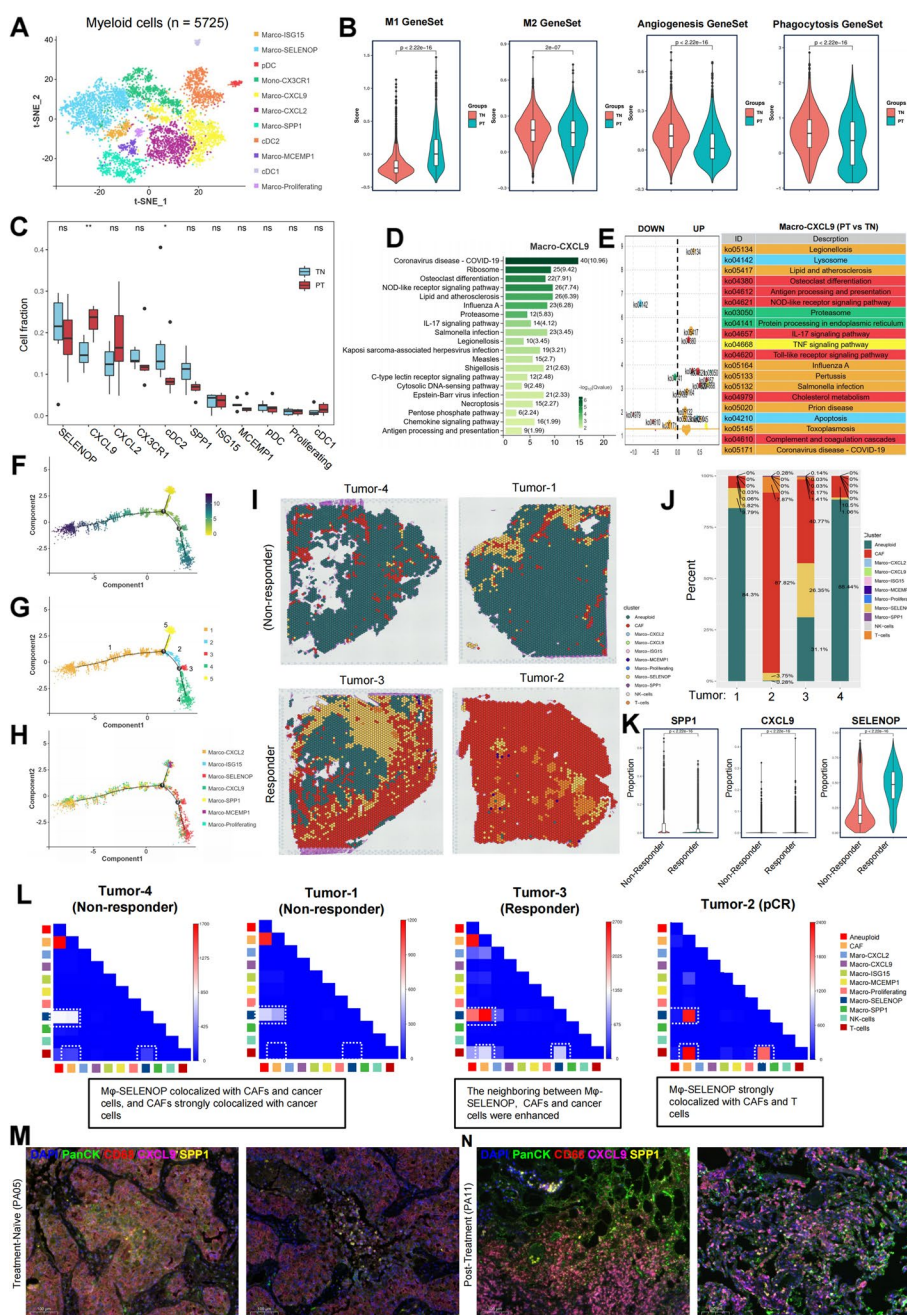


**Fig. 6** (See legend on previous page.)

demonstrated for each subgroup, and the distribution of cells in the PT group exhibited notable progression toward the branch ends (Figure S9H, S9I). These findings suggest that the combination treatment facilitated the differentiation process of macrophages toward Mφ-CXCL9 and Mφ-SELENOP. To validate the cell differentiation tree obtained from Monocle 2 analysis, a differentiation trajectory map of macrophages was constructed via Slingshot software (Figure S9J, Figure

S9K). The results demonstrated that the starting point of cellular differentiation was observed in Mφ-MCEMP, which was in accordance with the initial stage identified by Monocle2 analysis. Furthermore, two distinct lineage trajectories were identified for macrophages. The first lineage trajectory originated from Mφ-SELENOP and ended in Mφ-CXCL9. The second trajectory passed through Mφ-SPP1 and rooted in Mφ-proliferation. The cell trajectories predicted by Slingshot and Monocle

2 both originated from M $\phi$ -MCEMP and ended with M $\phi$ -CXCL9 as one of the terminations.

We also studied genes that exhibited dynamic expression with the development of macrophages, 1771 genes were identified to exhibit dynamic changes in line with cellular differentiation into different branches (Figure S9L). The genes were grouped into 5 clusters on the basis of changes in expression, and KEGG analysis was performed to study the functions enriched by the gene clusters. We found that during differentiation from state 5 to state 1 (M $\phi$ -CXCL9), the expression of chemokines and proinflammatory factors such as CXCL2, CXCL3, CXCL8, CCL3, CCL4, NFKBIA, TNFAIP3, HSPA1A, HSPA1B, and HSP90AA1 was significantly elevated. SELENOP was highly expressed with the trajectory from state 5 to state 4, indicating the differentiation of M $\phi$ -SELENOP in that branch. In addition, during the cellular differentiation of M $\phi$ -SELENOP, the expression of MHC genes and CD74 increased.

The RCTD algorithm was employed for the spatial annotation of macrophage subpopulations and other major cell subpopulations in NSCLC tissue sections (Fig. 6I). Tumor tissue 2 exhibited substantial infiltration of T cells, accompanied by a considerable number of M $\phi$ -SELENOP subpopulations. In tumor tissue 3, a significant number of M $\phi$ -SELENOP subpopulations were observed in proximity to malignant epithelial cells, along with T cells (Fig. 6J). The spatial data indicated that M $\phi$ -SELENOP subpopulations constituted the majority of all the macrophage subpopulations. The distributions of CXCL9, SPP1, and SELENOP macrophages between responders and non-responders were also compared, and the level of SELENOP and CXCL9 cells was found to be dramatically increased in responders, while the level of SPP1 cells was decreased in responders (Fig. 6K). We conducted spatial neighboring analysis of macrophage subpopulations, T cells, NK cells, malignant epithelial cells, and CAFs on the basis of spatial transcriptomic data from four NSCLC tissue sections. M $\phi$ -SELENOP cells colocalized with CAFs, T cells and tumor cells, whereas in the pCR tissue, the cl-localization of M $\phi$ -SELENOP cells and tumor cells disappeared as the number of tumor cells decreased (Fig. 6L). The spatial colocalization of M $\phi$ -SELENOP, CAFs, T cells, and tumor cells indicated the reconstruction of the TME in response to chemoimmunotherapy. To experimentally investigate the reshaping of macrophages in NSCLC tumors, we employed multiple immunofluorescence staining for the macrophage subpopulations SPP1 and CXCL9 in conjunction with malignant epithelial cells in NSCLC tissues with or without combined therapy (Fig. 6M, N). Our findings revealed a notable increase in the proportion of macrophages (CD68) in NSCLC tissues

following combination therapy. Furthermore, the spatial localization of macrophages was markedly restricted to lung cancer tissues prior to immunotherapy. However, in lung cancer tissues following combination therapy, CXCL9 + SPP1 + macrophages were not only widely distributed but also more closely adjacent to tumor cells (PanCK).

#### **Chemoimmunotherapy reshaped the TME by changing the proportion of matrix CAFs and inflammatory CAFs and enhancing the activity of antigen-presenting CAFs**

Cancer-associated fibroblasts (CAFs) are highly important within the microenvironment of solid tumors and are closely associated with tumor growth, metastasis and responsiveness to immunotherapy. A total of 2801 fibroblasts were obtained from 12 NSCLC patients, which were then divided into 5 subsubpopulations on the basis of classical marker genes, namely, antigen-presenting CAFs (apCAFs), inflammatory CAFs (iCAFs), matrix CAFs (mCAFs), metabolic CAFs (meCAFs) and proliferative CAFs (pCAFs) (Fig. 7A). The marker genes of each fibroblast subsubpopulation are presented, and the Kyoto Encyclopedia of Genes and Genomes (KEGG) method was used to analyze the differentially upregulated genes of the subsubpopulations to identify their biological functions (Fig. 7B). Furthermore, the proportions of each fibroblast subsubpopulation in different samples and subgroups were analyzed (Fig. 7C, Figure S10A). The results demonstrated that the proportion of apCAFs was significantly lower in the PT group than in the control group, whereas the proportion of meCAFs was significantly greater. These findings suggest that the combined therapy significantly altered the distribution and function of the fibroblast population in the tumor microenvironment and that these changes might be associated with immunotherapy responsiveness. In contrast, a greater proportion of iCAFs was observed in PA10 samples (pCR sample), indicating that iCAFs may play a role in tissue reconstruction following tumor necrosis.

We next investigated the functions of CAF subclusters (Fig. 7B). mCAFs highly expressed ECM-related genes and were found to be associated with ECM-receptor interactions and the TGF-beta signaling pathway. iCAFs expressed proinflammatory genes, and KEGG analysis suggested that the genes whose expression was upregulated in iCAFs were enriched in "Pathways in cancer", "Small cell lung cancer", and "PI3K-Akt signaling pathway", indicating an oncogenic role of iCAFs. KEGG analysis revealed that "DNA replication", "cell cycle", and "cell senescence" were enriched with the marker genes of pCAFs. Furthermore, the GSVA method was employed to conduct a comparative analysis of the functional enrichment of the five subpopulations of CAF cells

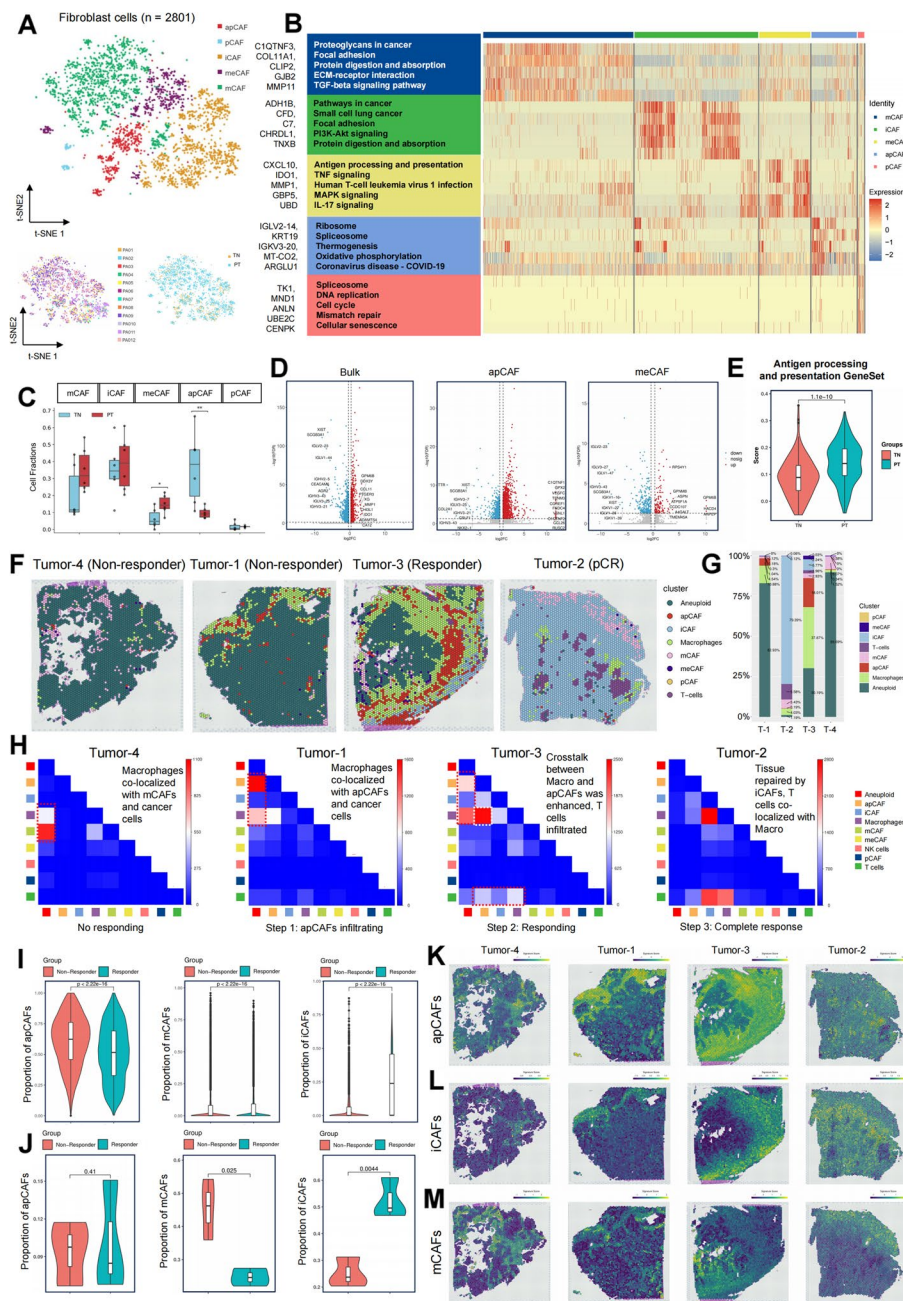


**Fig. 7** Chemoimmunotherapy reshaped the TME by changing the proportion of matrix CAFs to inflammatory CAFs and enhancing the activity of antigen-presenting CAFs. **A** Reclustering of cancer-associated fibroblasts into 8 subpopulations shown by a t-SNE plot (upper), the distribution of CD4 + T cells in each sample (lower left), and the treatment-naïve and posttreatment groups (lower right). **B** Heatmaps showing the significantly upregulated genes in all CAF subclusters. **C** Box plot showing the comparison of the fractions of CD4 + T-cell subtypes between TNs and PTs (Wilcoxon, \* indicates  $P < 0.05$ , \*\* indicates  $P < 0.01$ ). **D** Volcano maps showing the DEGs in bulk CAFs, apCAFs, and meCAFs, and the top 10 DEGs are labeled. **E** Violin plots comparing the antigen-presentation gene signatures of CAFs in the TN and PT groups ( $P$  values from Wilcoxon tests). **F** Spatial annotation of CAF subtypes, tumor cells, macrophages, and T cells in 4 NSCLC tumor sections inferred via the RCTD algorithm. **G** The percentages of each cell type identified in the NSCLC sections. **H** Heatmap showing the neighboring relationships between CAF subtypes and tumor cells, T cells, and macrophages in each NSCLC section. The pairs of cells that show significant changes in spatial distance with increasing sensitivity to chemoimmunotherapy are within the white dotted line. The number on the bar indicates the number of cells that have neighboring relationships. **I** Violin plots showing the proportions of apCAFs (left), mCAFs (middle), and iCAFs (right) in non-responders and responders ( $P$  value). **J** Violin plots showing the proportions of apCAFs (left), mCAFs (middle), and iCAFs (right) in non-responders (NMPR patients,  $n = 3$ ) and responders (MPR and pCR patients,  $n = 3$ ), data from scRNA-seq ( $P$  values determined by Wilcoxon tests). Signature scores of apCAFs (**K**), iCAFs (**L**) and mCAFs (**M**) in each NSCLC section were calculated and inferred by heatmaps. Light green color indicates high score, dark blue color indicates low score

(Figure S10B). This analysis revealed that iCAFs were significantly enriched in the Notch pathway and the angiogenic pathway. In contrast, mCAFs were significantly enriched in the WNT pathway and EMT pathway. Additionally, apCAFs were significantly enriched in the PI3K-Akt pathway. pCAFs were enriched in genes related to the cell cycle, mitosis, and DNA damage repair. The most functionally distinctive meCAFs were found to be significantly enriched in proinflammatory pathways, including the chemokine and interferon pathways, as well as in the EMT and TGF-beta pathways.

Furthermore, the genes differentially expressed in subpopulations of CAFs between the TN and PT groups were analyzed to evaluate the effects of combination therapy on cellular function. Our findings revealed 995 upregulated genes and 2313 downregulated genes in CAFs, 1191 upregulated genes and 633 downregulated genes in apCAFs, and 128 upregulated genes and 255 downregulated genes in meCAFs (Fig. 7D). The upregulated genes in each CAF subcluster in the PT group are shown in bubble plots (Figure S10C, Table S13). Furthermore, the antigen processing and presentation signatures of apCAFs were analyzed, and the results revealed that apCAFs in the PT group presented significantly enhanced antigen-presenting function (Fig. 7E). We evaluated the changes in the biological functions of the CAF subclusters by analyzing the DEGs via KEGG analysis. The enrichment results revealed a diversity of pathways related to the DEGs, and we identified several of these pathways. The results of the KEGG analysis revealed that the pathways associated with TNF signaling, p53 signaling, NOD-like receptor signaling, apoptosis, and TGF-beta signaling were increased in apCAFs but inhibited in the cell cycle, non-small cell lung cancer, and notch signaling pathways (Figure S10D). The expression of meCAFs was found to be increased in pathways related to protein export, the proteasome, and oxidative phosphorylation and inhibited in pathways related to the spliceosome, protein processing in the endoplasmic reticulum, and thermogenesis (Figure S10E). In addition, iCAFs inhibited several hallmark pathways, such as the TGF-beta signaling, WNT signaling, Hippo signaling, and mTOR signaling pathways, suggesting the transition of iCAFs to an antitumor phenotype (Figure S10F). GSEA revealed several pathways related to the immune response; however, the pathways associated with natural killer cell-mediated cytotoxicity, BCR signaling, neutrophil extracellular trap formation, NF-kB signaling apCAFs and meCAFs were inhibited in apCAFs and meCAFs after combined therapy (Figure S10G, Figure S10H).

To elucidate the interrelationship between CAF subpopulations and other key cell types in tissue sections, we spatially mapped the CAF subpopulations with

malignant epithelial cells, macrophages, and T cells via the RCTD algorithm (Fig. 7F, G) and performed a neighboring analysis to evaluate the spatial relationships between the cells (Fig. 7H). As immunotherapeutic sensitivity increases (from nonresponder to pCR), apCAFs co-localized with macrophages (mostly SELENOP-macrophages), accumulated in tumor boundaries and infiltrated within tumor regions, indicating the cooperative roles of apCAFs and SELENOP-macrophages in the anti-tumor activity induced by immunotherapy. In addition, with the decreasing of malignant areas, iCAFs were found to be accumulated in the non-malignant areas. Furthermore, matrix CAFs had the closest spatial relationships with tumor cells in the nonresponder region, especially in tumor-4, which exhibited the worst response in all the ST samples. These findings indicate that matrix CAFs might support an immunosuppressive TME, while iCAFs were aggregated in non-tumor regions. Next, proportions of CAFs subclusters between responders and non-responders were analyzed, and results showed that the levels of iCAFs and meCAFs were significantly increased in responders, however the levels of apCAFs, mCAFs and pCAFs were notably decreased in responders (Fig. 7I, Figure S10I, Figure S10J). Data from scRNA-seq suggested an elevation of iCAFs and a decrease in the proportion of mCAFs in responders (Fig. 7J). We scored the distributions of apCAFs (Fig. 7K), iCAFs (Fig. 7L) and mCAFs (Fig. 7M) in each NSCLC section, and the results demonstrated that apCAFs and iCAFs mostly aggregated in non-malignant areas, while mCAFs were widely distributed in malignant areas, which further supported their roles in the TME. mCAFs were more correlated with an immunosuppressive microenvironment and an unfavorable sensitivity to immunotherapy, while iCAFs were accumulated in an immune activated and non-malignant areas, suggesting its critical role in TME reconstruction after immunotherapy.

#### **Effective chemoimmunotherapy enhanced the cell-cell communications between SELENOP-macrophages, apCAFs and T cells in NSCLC tumor microenvironment**

As demonstrated in the former analyses, there is a significant enrichment of SELENOP macrophages and apCAFs in immunotherapy-sensitive tissues at the tumor boundaries, as well as in non-tumor tissues, and these cells demonstrate significant spatial co-localization relationships. Furthermore, the proportion of SELENOP macrophages is significantly increased after immunotherapy. We therefore hypothesized that SELENOP macrophages and apCAFs play an important role in immunotherapy-induced immune activation and immune cell recruitment. Next, we investigated the cell-cell communication patterns between SELENOP macrophages, apCAFs, and

T cells in responders and non-responders basing on the data from spatial transcriptomic analysis, in order to find out how these cells interact with each other when responding to chemoimmunotherapy.

CD4+ and CD8+ T cells were re-clustered by cellular functions. CD4+ T cells were re-clustered into Helper, Memory, Naïve and Treg, and CD8+ T cells were re-clustered into Effector, Exhausted, Memory and Naïve. RCTD algorithm was employed to annotate the T cell subclusters, apCAFs and SELENOP-macrophages on each section, and neighboring analysis was subsequently performed on these three groups of cells. Results demonstrated no significant co-localization between T cells and other two cell types in non-responders, while in responders CD4+ memory and Naïve cells showed some spatial correlation with apCAFs and SELENOP-macrophages (Fig. 8A, B). We next investigated the cell–cell communication patterns by using CellPhoneDB algorithm, and the results demonstrated that the T cell subcluster that communicated with SELENOP macrophages as well as apCAFs in the non-responder was CD4+ memory cells. In responders, a variety of T cell clusters were observed to communicate with SELENOP macrophages and apCAFs, including CD4+ Helper, CD4+ Naïve and CD8+ Naïve T cells. This finding suggests that effective immunotherapeutic responses strengthened the communications between T cells and these two cell types. (Fig. 8C). The differential signaling pathways connected T cells, SELENOP-macrophages and apCAFs between responders and non-responders were analyzed, and the top 20 pathways in each group were shown by a bar plot (Fig. 8D, Table S14).

We next investigated the outgoing and incoming signaling patterns in the communication network of T cells, SELENOP-macrophages and apCAFs. The results showed that the variety of communication patterns in this network was significantly increased in responders, as the the outgoing and incoming signals from and into CD8 Naïve T cells were significantly enhanced (Fig. 8E, F). In addition, in non-responders, CD4+ memory T cells were the dominant cell type that sending signals, while in responders, SELENOP-macrophages and apCAFs were dominant in sending signals, and CD4 Naïve T cells received strong incoming signals. We also found that CD8+ Naïve T cells sent and received signals through pathways including interleukin, transforming growth factor and HLA in this network. The top 15 signaling pathways with the highest possibilities in non-responders (Fig. 8G, Table S15) and responders (Fig. 8H, Table S16) were shown by bubble plots. In non-responders, Apolipoprotein pathway connected SELENOP-macrophages with the other cell clusters in the network, while Annexin connected the signaling from CD4 Memory T cells to the other cell clusters. In responders, cholesterol pathway connected the signals sent from SELENOP-macrophages to the other cell clusters in the network, while interferon pathway connected signals sent from CD4 Helper T cells to the other cell clusters. SELENOP-macrophages played the central role in Apolipoprotein signaling network in non-responders (Fig. 8I), and APOE-TREM2 pair is the key ligand-receptor pair in this pathway, the signaling network was visualized and plotted in tumor-1 (Fig. 8K) and tumor-4 (Fig. 8L). In

(See figure on next page.)

**Fig. 8** Effective chemoimmunotherapy changes the communication patterns between SELENOP-macrophages, apCAFs and T cell subclusters.

**A** Heatmap showing the neighboring relationships between T cell subclusters, SELENOP-macrophages and apCAFs. The number on the bar indicates the number of cells that have neighboring relationships. **B** Spatial annotation of indicated T cell subclusters, SELENOP-macrophages and apCAFs in 4 NSCLC tumor sections inferred via the RCTD algorithm. **C** Circle plots showing the differential number of interactions and strength in the network of T cell subclusters, SELENOP-macrophages and apCAFs, between non-responders and responders, inferred via CellPhoneDB algorithm. The arrows indicate the direction of signaling flow. Red color or blue color indicate the strengthening or weakening of the signaling flow, respectively. Thickness of the lines indicates the number (left) and strength (right) of the interactions. **D** Bar graph showing the differential signaling pathways between non-responders and responders. The selected significant signaling pathways were ranked top 20 on the basis of their differences in overall information flow within the inferred networks between non-responders and responders. The pathways colored in red are more enriched in non-responders, and those colored in green are more enriched in responders. Heatmaps showing the strength of outgoing (**E**) and incoming (**F**) signaling patterns with the network between non-responders and non-responders. Green color indicates the strengthening of signaling. The top 15 significant pathways within the cell–cell communication network in non-responders (**G**) and responders (**H**) were shown by bubble plots. Indicated pathways and relative communication patterns were colored in red or blue. The scale of the bubble indicates the p-values, and color indicates the expression level of ligands and receptors contributed to the pathways. **I** The social network model of Apolipoprotein pathway in non-responders was shown by a heat plot. The Color indicates the importance of indicated cell cluster in the network. **J** The ligand-receptor pair that contributed to Apolipoprotein pathway was shown by a bubble plot. The color indicates the communication possibility. **K, L** The spatial distribution of indicated cell clusters and communication patterns within the network in non-responder sections were inferred by CellPhoneDB. **M** The social network model of Cholesterol pathway in responders was shown by a heat plot. The Color indicates the importance of indicated cell cluster in the network. **J** The ligand-receptor pairs contributed to Cholesterol pathway were shown by a bubble plot. The color indicates the communication possibility. **K, L** The spatial distribution of indicated cell clusters and communication patterns within the network in responder sections were inferred by CellPhoneDB

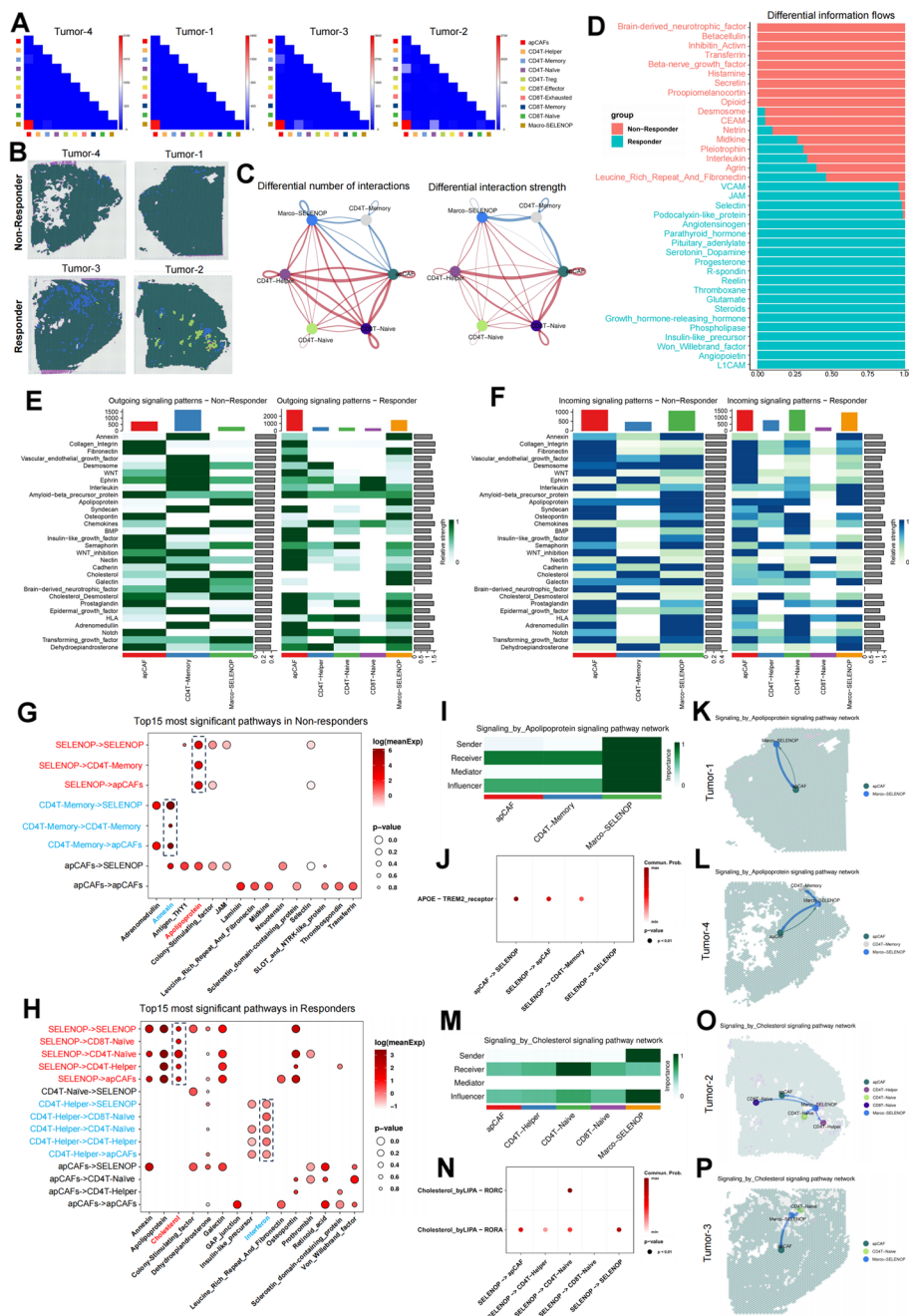


**Fig. 8** (See legend on previous page.)

responders, cholesterol is the most significant pathway that linked the signals from SELENOP-macrophages to other cell clusters in the network (Fig. 8M), and the pairs of LIPA-RORC and LIPA-RORA were the key ligand-receptor pairs in the pathway (Fig. 8N), the cholesterol signaling network in responders were plotted and visualized (Fig. 8O, P).

**Discussion**

The emergence of immunotherapies, including immune checkpoint blockade and engineered T-cell therapy, has brought a new era of hope to cancer patients. The potential of neoadjuvant immunotherapy extends beyond the inhibition of unresectable tumors; it also presents opportunities for surgical resection. Consequently, neoadjuvant

immunotherapy has emerged as a highly efficacious therapeutic strategy for NSCLC and has even become a first-line therapeutic option. Nevertheless, the precise effective rate remains uncertain, prompting the conduction of numerous studies targeting immunotherapy responsiveness with the aim of elucidating the relationship between tumor heterogeneity and immunotherapy responsiveness. The application of single-cell sequencing and spatial transcription technologies enables the dissection of the tumor immune microenvironment at the single-cell level. In this study, we enrolled 6 NSCLC patients who underwent neoadjuvant immunotherapy followed by surgical resection and 6 patients who directly underwent surgical resection of the tumor. Tumor tissues were obtained from both groups and subjected to single-cell sequencing and spatial transcriptome sequencing. The dynamic changes in the cellular composition, spatial distribution, gene expression and cellular communication between the two groups of samples were identified, and a spatial transcriptomic atlas of the NSCLC TME before and after immunotherapy was generated. Our study provides an in-depth analysis of the reshaping of the NSCLC TME caused by neoadjuvant immunotherapy.

Clonal expansion and infiltration of tumor-associated lymphocytes represent critical aspects of the response to immunotherapy [58]. A number of previous studies have conducted in-depth analyses of treatment-naïve NSCLC tissues, providing extensive baseline information [59–61]. However, profiling of cancer tissues after immunotherapy remains insufficiently explored. The data demonstrated that immunotherapy resulted in a reduction in the proportion of Th17 CD4+ T cells and the suppression of gene expression associated with the pathway of Th17 cell differentiation. Th17 cells are crucial for host resistance to pathogens [62]; however, Th17-secreted IL-17 and IL-22 are postulated to facilitate tumor growth [63]. Furthermore, in NSCLC, high expression of Th17 cell-associated genes has been linked to a poor response to anti-PD-1 therapy [64]. Our data demonstrated that the proportion of Th17 cells and the expression of related genes were reduced in the PT group. Th17 cells exhibited a significantly low exhaustion signature, and the results of the analysis of the cellular developmental trajectory indicated that Th17 cells were located not at the end but throughout one branch of the differentiation trajectory. Additionally, the differentiation path of Th17 cells overlaps with that of Trm cells, which is the opposite of that of Tregs. The data demonstrated that immunotherapy significantly decreased the proportion of KLRG1+CD8+ T cells in NSCLC tumors. KLRG1+CD8+ T cells are a subtype of cytotoxic effector T cells that are induced by strong T-cell receptors as well as inflammatory signals [65, 66]. PD-1 blockade

in combination with chemotherapy enhances the intra-tumor infiltration of KLRG1+CD8+ T cells, which in turn leads to an improved prognosis in NSCLC patients [67]. However, KLRG+CD8+ T cells reportedly exhibit impaired antitumor immunity in a variety of cancers, including NSCLC [67, 68]. Furthermore, KLRG has been shown to recognize E-cadherin and to inhibit the activity of T cells and NK cells [69], thereby inducing immune escape [67, 70]. We propose that the lower level of KLRG1+CD8+ T cells in the PT group is attributable to the impact of chemoimmunotherapy on the cellular differentiation of CD8+ T cells and that the combined therapy stimulated the progression of cell differentiation, whereas KLRG1+CD8+ T cells were located at the initial stage of the developmental trajectory. However, the association between the infiltration of KLRG+ T cells and immunotherapy response remains to be elucidated.

The intratumor infiltration of plasma cells indicates a favorable response to PD-1 blockade [71, 72], and the presence of a high abundance of follicular B cells in tumor tissue has been associated with sensitivity to anti-tumor therapy and favorable outcomes [73]. Although our single-cell data revealed a notable decrease in the proportion of plasma cells following treatment, spatial transcriptomic data revealed substantial B-cell infiltration in pCR and responder tumor tissues, whereas B-cell infiltration was largely absent in nonresponder tissues. Moreover, diverse B-cell subtypes, especially those in TLS regions, including GCB and follicular B cells, were observed in pCR tissue. A substantial number of IgG+ plasma cells are present in pCR tissue, which we believe is a strong predictor of immunotherapy responsiveness.

Tumor associated macrophages represent a prominent element of the TME, exerting a profound influence on tumor cell growth and treatment resistance [74, 75]. Our single-cell data revealed a notable increase in the proportion of CXCL9+ macrophages following treatment, whereas the proportions of SPP1+ and SELENOP+ macrophages tended to decrease. Furthermore, spatial transcriptome analysis revealed that SELENOP+ macrophages were extensively distributed in NSCLC tissues, with the highest proportion of distribution in responder tissues. In both pCR and responder tissues, SELENOP macrophages exhibited notable spatial colocalization with T cells, indicating a close relationship between them. Notably, in responder tissues, SELENOP+ macrophages, in conjunction with CAFs, constitute a rampart-like structure that separates tumor cells from T cells and B cells. The literature demonstrates that ICB therapy induces CXCL9 secretion from macrophages and promotes the immune infiltration of CD8+ T cells [76]. Consequently, increased CXCL9 secretion is associated with

favorable immunotherapy responsiveness [76]. Recently, the ratio of CXCL9 to SPP1 gene expression has been proposed as a means of defining TAM polarization and evaluating global changes in the tumor microenvironment and patient prognosis [77]. The data revealed a significant increase in the proportion of CXCL9+ macrophages and a notable reduction in the SPP1+ macrophages fraction in response to chemoimmunotherapy. The overall TMA polarization was found to be more M1-like in the PT group, indicating that the functions of TAMs had undergone a switch toward proinflammatory and antitumor activity. Furthermore, Monocle 3 revealed that CXCL9 and SPP1 cells are located at the ends of two distinct branches, indicating disparities in cell fate and biological functions. Our analyses revealed a substantial number of SELENOP+ macrophages, which were significantly clustered around tumor cells in responder tissues. The function of SELENOP+ macrophages remains unclear; however, Wang et al. proposed that they may play an antitumor role [53]. Our data indicated that, in addition to their involvement in cellular metabolism, SELENOP+ macrophages may also play an antigen-presenting role, as evidenced by their high expression of the MHC I and MHC II genes. The significant colocalization observed with T cells, as revealed by our spatial transcriptomic analysis, further suggested that these cells may be involved in antigen presentation and the induction of T-cell aggregation.

Fibroblasts represent a significant component of the cellular stroma. Cancer-associated fibroblasts exhibit considerable heterogeneity and assume a variety of roles within the TME. These roles include reshaping the TME by promoting tumor growth and inflammation, as well as remodeling the extracellular matrix. Our data revealed a notable decrease in the proportion of apCAFs in the PT group, whereas the proportion of meCAFs markedly increased. Additionally, the proportion of mCAFs tended to increase. Spatial transcriptomic data indicated that apCAFs were significantly present in responder tissues and strongly colocalized with SELENOP+ TAMs, suggesting that they may work together to conduct antigen presentation. In contrast, in pCR tissue, iCAFs were the predominant CAF subtype, accounting for the majority of the tissue. This finding is consistent with the findings of Cords et al., who reported that iCAFs are associated with an inflammatory TME and a good prognosis for NSCLC patients [78]. In contrast, the infiltration of apCAFs was extremely limited in nonresponder tissues. Furthermore, meCAFs were observed to colocalize with mCAFs and to be present closely to tumor cells. mCAFs promote the invasiveness of tumors and inhibit immune infiltration [78, 79]. meCAFs have been demonstrated to participate in glycolysis and alanine, aspartate,

and glutamate metabolism [80]. Our data indicated that meCAFs expressed a range of genes involved in immune regulation, including MHC I genes, STAT genes, and cytokines. Compared with other CAF subtypes, meCAFs were significantly enriched in pathways associated with epithelial-to-mesenchymal transition (EMT), transforming growth factor beta (TGF-beta), Janus kinase-signal transducers and activators of transcription 3 (JAK-STAT3), interferon, and tumor necrosis factor (TNF) signaling. These findings suggest that meCAFs may play a complicated and activated role in the TME of NSCLC. To date, no studies have reported the infiltration and colocalization of meCAFs and mCAFs in tumor tissues. It may be hypothesized that mCAFs work in conjunction with meCAFs to regulate the reconstruction of the extracellular matrix, thereby creating an immunosuppressive microenvironment. Our data from scRNA-seq and ST analysis suggested that the accumulation of iCAFs and less distribution of mCAFs in the TME correlated with the favorable responsiveness to chemoimmunotherapy.

NSCLC cells are derived from epithelial cells. The literature indicates that AT2 and club cells have the potential to develop into lung adenocarcinoma cells, whereas basal cells and club cells can develop into lung squamous cell carcinoma cells [81, 82]. Our study identified 8 distinct epithelial cell subtypes and classified them as diploid or aneuploid cells on the basis of CNVs. The epithelial cells exhibited strong heterogeneity. The comparison revealed that approximately 70% of the aneuploid cells were derived from basal cells, 4.99% from AT2 cells, and 4.42% from club cells, whereas the diploid cells were derived from a wide range of epithelial cells (33% from basal cells, 22.39% from AT2 cells, and 9.17% from club cells). These findings suggested that NSCLC cells might be predominantly differentiated from basal cells. By performing cell trajectory analysis, we identified genes that exhibited dynamic changes with pseudotime progression. Our findings revealed that the expression of the KRAS gene increased with the transformation of epithelial cells to malignant epithelium. Additionally, we observed a similar trend in the expression of keratin genes, including KRT 14, 16, 17 and 19. KRT19 has been recognized to play a prognostic role in NSCLC patients [83, 84], and KRT genes are reportedly associated with the estrogen response [85]. This finding suggests the possibility of simultaneous activation of the estrogen receptor pathway alongside the malignant transformation of epithelial cells. Elevated serum estrogen levels have been reported in NSCLC patients with poor responses to immunotherapy [20], which suggests that the activity of the estrogen pathway may be associated with unresponsiveness to immunotherapy.

This study is not without limitations. First, the neo-adjuvant therapy employed in the study consisted of immunotherapy in conjunction with chemotherapy rather than immunotherapy alone. Consequently, the observed alterations in the tumor immune microenvironment are attributable not only to immunotherapy but also to the response to chemotherapy. Second, although 4 NSCLC tumor tissue sections were included in this study for spatial transcription analysis, there is still a lack of treatment-naïve tissue samples for the control. Third, the sample size was insufficient to support the grouping of patients after neoadjuvant therapy, thereby hindering further investigation into the features of TME changes associated with immunotherapy responsiveness in the PT group. Furthermore, the considerable individual variability observed in this study reflected the tumor heterogeneity among NSCLC patients. However, this also contributed to the absence of statistically significant findings when comparing between groups, such as the differences in TCR colony expansion between groups. Additionally, individual patient characteristics, tumor stage, and the relatively limited sample size may have influenced the results. Fourth, although 4 TLS regions were identified in this study, further analysis of the TLS regions, such as cell-to-cell distance, genomic alterations and biological functions, should be conducted.

In conclusion, our study revealed dynamic changes in the tumor microenvironment subsequent to neoadjuvant chemoimmunotherapy. The SELENOP-macrophages were found to be aggregated within the tumor boundary and TLSs regions, and the interaction between SELENOP-macrophages and apCAFs plays a critical role in the anti-tumor immunity and reconstruction of the TME induced by successful chemoimmunotherapy. Distribution of CD4+ Treg T cells and mCAFs indicated an immunosuppressive TME, while the accumulation of CD4+ Th17 T cells and iCAFs could act as a positive marker for the sensitivity to chemoimmunotherapy.

#### Abbreviations

NSCLC	Non-small cell lung cancer
ICB	Immune checkpoint blockage
PFS	Progression free survival
OS	Overall survival
RR	Response rate
PD-L1	Programmed cell death ligand 1
TME	Tumor microenvironment
ECM	Extracellular matrix
TIB	Tumor infiltrating B cells
MPR	Major pathological response
NMPR	Non-major pathological response
pCR	Pathological complete response
FFPE	Formalin-fixed paraffin-embedded
ST	Spatial transcriptome
UMI	Unique molecular identifiers
mIHC	Multiplex immunohistochemistry
IHC	Immunohistochemistry
TN	Treatment naïve

PT	Post treatment
CT	Computed tomography
RCTD	Residual convolutional neural network with the transformer decoder
H&E	Hematoxylin–eosin
TLS	Tertiary lymphoid structures
CNV	Copy number variations
TKI	Tyrosine kinase inhibitors
t-SNE	T-distributed stochastic neighbor embedding
DEGs	Differentially expressed genes
TCR	T cell receptor
BCR	B cell receptor

## Supplementary Information

The online version contains supplementary material available at <https://doi.org/10.1186/s12943-025-02287-w>.

Supplementary Material 1.

Supplementary Material 2.

#### Acknowledgements

We thank all the members of the research team for their generous support of this work, and we thank all the patients who participated in this study. We are grateful to Gene Denovo (Guangzhou, China) for assisting in the bioinformatics analysis in this study. We especially thank Dr. Kangping Song from Gene Denovo for his assistance and support in the study. Bioinformatic analysis was performed using Omicsmart, a dynamic real-time interactive online platform for data analysis (<http://www.omicsmart.com>). The graphic abstract was created by Figdraw (<https://www.figdraw.com>) with the authorization ID (PRPPI98f48).

#### Authors' contributions

X.C. and S.L. contributed equally to this work. X.C. and Y.S. conceived the project and designed the experiments. Y.S. and S.L. collected the samples and performed the sequencing experiments, and X.C. and S.L. processed the data and performed the experiments. X.C. wrote the manuscript. H.S., J.X., and Y.S. acquired funding. All the authors have read and approved the final manuscript.

#### Funding

Not applicable.

#### Data availability

All single-cell sequencing raw data from this study are available from the NCBI under accession number PRJNA1068179 by visiting <https://www.ncbi.nlm.nih.gov/bioproject/PRJNA1068179>. The spatial transcriptome sequencing raw data are available from the NCBI under accession number PRJNA1139087 by visiting <https://www.ncbi.nlm.nih.gov/bioproject/PRJNA1139087>. The public scRNA-seq data used in this study for validation are available from Gene Expression Omnibus, under accession number GSE207422 (<https://www.ncbi.nlm.nih.gov/geo/query/acc.cgi?acc=GSE207422>). The other resources used in this study are available upon request from the corresponding author.

#### Declarations

#### Ethics approval and consent to participate

This study was conducted in accordance with ethical standards and national and international guidelines. This study was approved by the Research Ethics Committee of China Medical University, and all patients provided written informed consent. The collection of patient samples and related experiments in this study were approved by the Medical Ethics Committee of the First Hospital of China Medical University (Authorization number: AF-SOP-07–1.2–01).

#### Competing interests

The authors declare no competing interests.

**Author details**

<sup>1</sup>Department of Urology, First Hospital of China Medical University, Shenyang, Liaoning Province 110001, China. <sup>2</sup>Department of Thoracic Surgery, First Hospital of China Medical University, Shenyang, Liaoning Province 110001, China. <sup>3</sup>Department of Gastrointestinal Surgery, First Hospital of China Medical University, Shenyang, Liaoning Province 110001, China. <sup>4</sup>Department of Rheumatology and Immunology, Shengjing Hospital of China Medical University, Shenyang, Liaoning Province 110004, China.

Received: 4 October 2024 Accepted: 28 February 2025

Published online: 09 April 2025

**References**

- Siegel RL, Giaquinto AN, Jemal A. Cancer statistics, 2024. *CA Cancer J Clin.* 2024;74(1):12–49.
- Bray F, Laversanne M, Sung H, et al. Global cancer statistics 2022: GLOBOCAN estimates of incidence and mortality worldwide for 36 cancers in 185 countries. *CA Cancer J Clin.* 2024;74(3):229–63.
- Herbst RS, Morgensztern D, Boshoff C. The biology and management of non-small cell lung cancer. *Nature.* 2018;553(7689):446–54.
- Reck M, Remon J, Hellmann MD. First-line immunotherapy for non-small-cell lung cancer. *J Clin Oncol.* 2022;40(6):586–97.
- Lahiri A, Maji A, Potdar PD, et al. Lung cancer immunotherapy: progress, pitfalls, and promises. *Mol Cancer.* 2023;22(1):40.
- Cortiula F, Reymen B, Peters S, et al. Immunotherapy in unresectable stage III non-small-cell lung cancer: state of the art and novel therapeutic approaches. *Ann Oncol.* 2022;33(9):893–908.
- Girard N, Bar J, Garrido P, et al. Treatment characteristics and real-world progression-free survival in patients with unresectable stage III NSCLC who received durvalumab after chemoradiotherapy: findings from the PACIFIC-R study. *J Thorac Oncol.* 2023;18(2):181–93.
- Forde PM, Spicer J, Lu S, et al. Neoadjuvant nivolumab plus chemotherapy in resectable lung cancer. *N Engl J Med.* 2022;386(21):1973–85.
- Chen Y, Yan B, Xu F, et al. Neoadjuvant chemoimmunotherapy in resectable stage IIIA/IIIB non-small cell lung cancer. *Transl Lung Cancer Res.* 2021;10(5):2193–204.
- Passaro A, Attili I, de Marinis F. Neoadjuvant chemotherapy plus immunotherapy in early-stage resectable non-small-cell lung cancer. *J Clin Oncol.* 2022;40(25):2871–7.
- Forde PM, Chaft JE, Smith KN, et al. Neoadjuvant PD-1 blockade in resectable lung cancer. *N Engl J Med.* 2018;378(21):1976–86.
- Rahim MK, Okholm T, Jones KB, et al. Dynamic CD8(+) T cell responses to cancer immunotherapy in human regional lymph nodes are disrupted in metastatic lymph nodes. *Cell.* 2023;186(6):1127–1143.e18.
- He J, Xiong X, Yang H, et al. Defined tumor antigen-specific T cells potentiate personalized TCR-T cell therapy and prediction of immunotherapy response. *Cell Res.* 2022;32(6):530–42.
- Kong J, Ha D, Lee J, et al. Network-based machine learning approach to predict immunotherapy response in cancer patients. *Nat Commun.* 2022;13(1):3703.
- Deng H, Zhao Y, Cai X, et al. PD-L1 expression and tumor mutation burden as pathological response biomarkers of neoadjuvant immunotherapy for early-stage non-small cell lung cancer: a systematic review and meta-analysis. *Crit Rev Oncol Hematol.* 2022;170: 103582.
- Pitt JM, Marabelle A, Eggermont A, Soria JC, Kroemer G, Zitvogel L. Targeting the tumor microenvironment: removing obstruction to anticancer immune responses and immunotherapy. *Ann Oncol.* 2016;27(8):1482–92.
- Baharom F, Ramirez-Valdez RA, Khalilnezhad A, et al. Systemic vaccination induces CD8(+) T cells and remodels the tumor microenvironment. *Cell.* 2022;185(23):4317–4332.e15.
- Kim R, An M, Lee H, et al. Early tumor-immune microenvironmental remodeling and response to first-line fluoropyrimidine and platinum chemotherapy in advanced gastric cancer. *Cancer Discov.* 2022;12(4):984–1001.
- Hui Z, Zhang J, Ren Y, et al. Single-cell profiling of immune cells after neoadjuvant pembrolizumab and chemotherapy in IIIA non-small cell lung cancer (NSCLC). *Cell Death Dis.* 2022;13(7):607.
- Hu J, Zhang L, Xia H, et al. Tumor microenvironment remodeling after neoadjuvant immunotherapy in non-small cell lung cancer revealed by single-cell RNA sequencing. *Genome Med.* 2023;15(1):14.
- Chang JY, Lin SH, Dong W, et al. Stereotactic ablative radiotherapy with or without immunotherapy for early-stage or isolated lung parenchymal recurrent node-negative non-small-cell lung cancer: an open-label, randomised, phase 2 trial. *Lancet.* 2023;402(10405):871–81.
- Yi L, Xu Z, Ma T, et al. T-cell subsets and cytokines are indicative of neoadjuvant chemoimmunotherapy responses in NSCLC. *Cancer Immunol Immunother.* 2024;73(6):99.
- Hou L, Zhang S, Yu W, et al. Single-cell transcriptomics reveals tumor-infiltrating B cell function after neoadjuvant pembrolizumab and chemotherapy in non-small cell lung cancer. *J Leukoc Biol.* 2023 : qjad138 [pii].
- Gungabeesoon J, Gort-Freitas NA, Kiss M, et al. A neutrophil response linked to tumor control in immunotherapy. *Cell.* 2023;186(7):1448–1464.e20.
- Hellmann MD, Chaft JE, William WN Jr, et al. Pathological response after neoadjuvant chemotherapy in resectable non-small-cell lung cancers: proposal for the use of major pathological response as a surrogate endpoint. *Lancet Oncol.* 2014;15(1):e42–50.
- Blakely CM, Weder W, Bubendorf L, et al. Primary endpoints to assess the efficacy of novel therapeutic approaches in epidermal growth factor receptor-mutated, surgically resectable non-small cell lung cancer: A review. *Lung Cancer.* 2023;177:59–72.
- Seth S, Mallik S, Bhadra T, Zhao Z. Dimensionality reduction and louvain agglomerative hierarchical clustering for cluster-specified frequent biomarker discovery in single-cell sequencing data. *Front Genet.* 2022;13: 828479.
- Vanhersecke L, Brunet M, Guégan JP, et al. Mature tertiary lymphoid structures predict immune checkpoint inhibitor efficacy in solid tumors independently of PD-L1 expression. *Nat Cancer.* 2021;2(8):794–802.
- Sautès-Fridman C, Petitprez F, Calderaro J, Fridman WH. Tertiary lymphoid structures in the era of cancer immunotherapy. *Nat Rev Cancer.* 2019;19(6):307–25.
- Sun X, Liu W, Sun L, et al. Maturation and abundance of tertiary lymphoid structures are associated with the efficacy of neoadjuvant chemoimmunotherapy in resectable non-small cell lung cancer. *J Immunother Cancer.* 2022;10(11): e005531.
- Moser T, Akgün K, Proschmann U, Sellner J, Ziemssen T. The role of TH17 cells in multiple sclerosis: therapeutic implications. *Autoimmun Rev.* 2020;19(10): 102647.
- Chen CL, Wang Y, Huang CY, et al. IL-17 induces antitumor immunity by promoting beneficial neutrophil recruitment and activation in esophageal squamous cell carcinoma. *Oncimmunology.* 2017;7(1): e1373234.
- Lee YH, Chuah S, Nguyen P, et al. IFN $\gamma$ (-)/IL-17(+) CD8 T cells contribute to immunosuppression and tumor progression in human hepatocellular carcinoma. *Cancer Lett.* 2023;552: 215977.
- Marshall EA, Ng KW, Kung SH, et al. Emerging roles of T helper 17 and regulatory T cells in lung cancer progression and metastasis. *Mol Cancer.* 2016;15(1):67.
- Liu C, Liu R, Wang B, et al. Blocking IL-17A enhances tumor response to anti-PD-1 immunotherapy in microsatellite stable colorectal cancer. *J Immunother Cancer.* 2021;9(1): e001895.
- Chen X, Zhao J, Herjan T, et al. IL-17-induced HIF1 $\alpha$  drives resistance to anti-PD-L1 via fibroblast-mediated immune exclusion. *J Exp Med.* 2022;219(6): e20210693.
- Wu H, Tang X, Kim HJ, et al. Expression of KLRG1 and CD127 defines distinct CD8(+) subsets that differentially impact patient outcome in follicular lymphoma. *J Immunother Cancer.* 2021;9(7): e002662.
- Remmerswaal E, Hombrink P, Nota B, et al. Expression of IL-7Ra and KLRG1 defines functionally distinct CD8(+) T-cell populations in humans. *Eur J Immunol.* 2019;49(5):694–708.
- Braud VM, Allan DS, O'Callaghan CA, et al. HLA-E binds to natural killer cell receptors CD94/NKG2A. *B C Nat.* 1998;391(6669):795–9.
- Le Dréan E, Vély F, Olcese L, et al. Inhibition of antigen-induced T cell response and antibody-induced NK cell cytotoxicity by NKG2A: association of NKG2A with SHP-1 and SHP-2 protein-tyrosine phosphatases. *Eur J Immunol.* 1998;28(1):264–76.
- Boyington JC, Riaz AN, Patamawenu A, Coligan JE, Brooks AG, Sun PD. Structure of CD94 reveals a novel C-type lectin fold: implications

- for the NK cell-associated CD94/NKG2 receptors. *Immunity*. 1999;10(1):75–82.
42. van Hall T, André P, Horowitz A, et al. Monalizumab: inhibiting the novel immune checkpoint NKG2A. *J Immunother Cancer*. 2019;7(1):263.
  43. Herbst RS, Majem M, Barlesi F, et al. COAST: an open-label, phase II, multidrug platform study of durvalumab alone or in combination with oleclumab or monalizumab in patients with unresectable, stage III non-small-cell lung cancer. *J Clin Oncol*. 2022;40(29):3383–93.
  44. Liu X, Song J, Zhang H, et al. Immune checkpoint HLA-E:CD94-NKG2A mediates evasion of circulating tumor cells from NK cell surveillance. *Cancer Cell*. 2023;41(2):272–287.e9.
  45. Starzer AM, Berghoff AS. New emerging targets in cancer immunotherapy: CD27 (TNFRSF7). *ESMO Open*. 2020;4(Suppl 3):e000629.
  46. Parry EM, Lemvigh CK, Deng S, et al. ZNF683 marks a CD8(+) T cell population associated with anti-tumor immunity following anti-PD-1 therapy for Richter syndrome. *Cancer Cell*. 2023;41(10):1803–16.e8.
  47. Laumont CM, Banville AC, Gilardi M, Hollern DP, Nelson BH. Tumour-infiltrating B cells: immunological mechanisms, clinical impact and therapeutic opportunities. *Nat Rev Cancer*. 2022;22(7):414–30.
  48. Cabrera R, Lauss M, Sanna A, et al. Tertiary lymphoid structures improve immunotherapy and survival in melanoma. *Nature*. 2020;577(7791):561–5.
  49. Helmink BA, Reddy SM, Gao J, et al. B cells and tertiary lymphoid structures promote immunotherapy response. *Nature*. 2020;577(7791):549–55.
  50. Hao D, Han G, Sinjab A, et al. The single-cell immunogenomic landscape of b and plasma cells in early-stage lung adenocarcinoma. *Cancer Discov*. 2022;12(11):2626–45.
  51. Chen P, Zhao D, Li J, et al. Symbiotic macrophage-glioma cell interactions reveal synthetic lethality in PTEN-Null glioma. *Cancer Cell*. 2019;35(6):868–84.e6.
  52. Zhang Y, Du W, Chen Z, Xiang C. Upregulation of PD-L1 by SPP1 mediates macrophage polarization and facilitates immune escape in lung adenocarcinoma. *Exp Cell Res*. 2017;359(2):449–57.
  53. Wang C, Yu Q, Song T, et al. The heterogeneous immune landscape between lung adenocarcinoma and squamous carcinoma revealed by single-cell RNA sequencing. *Signal Transduct Target Ther*. 2022;7(1):289.
  54. De Filippo K, Dudeck A, Hasenberg M, et al. Mast cell and macrophage chemokines CXCL1/CXCL2 control the early stage of neutrophil recruitment during tissue inflammation. *Blood*. 2013;121(24):4930–7.
  55. Liu Y, Xiao J, Cai J, et al. Single-cell immune profiling of mouse liver aging reveals Cxcl2+ macrophages recruit neutrophils to aggravate liver injury. *Hepatology*. 2024;79(3):589–605.
  56. Nie F, Zhang J, Tian H, et al. The role of CXCL2-mediated crosstalk between tumor cells and macrophages in *Fusobacterium nucleatum*-promoted oral squamous cell carcinoma progression. *Cell Death Dis*. 2024;15(4):277.
  57. Cheng S, Li Z, Gao R, et al. A pan-cancer single-cell transcriptional atlas of tumor infiltrating myeloid cells. *Cell*. 2021;184(3):792–809.e23.
  58. Liu B, Hu X, Feng K, et al. Temporal single-cell tracing reveals clonal revival and expansion of precursor exhausted T cells during anti-PD-1 therapy in lung cancer. *Nat Cancer*. 2022;3(1):108–21.
  59. Wu F, Fan J, He Y, et al. Single-cell profiling of tumor heterogeneity and the microenvironment in advanced non-small cell lung cancer. *Nat Commun*. 2021;12(1):2540.
  60. Guo X, Zhang Y, Zheng L, et al. Global characterization of T cells in non-small-cell lung cancer by single-cell sequencing. *Nat Med*. 2018;24(7):978–85.
  61. Zheng L, Qin S, Si W, et al. Pan-cancer single-cell landscape of tumor-infiltrating T cells. *Science*. 2021;374(6574):abe6474.
  62. Knochelmann HM, Dwyer CJ, Bailey SR, et al. When worlds collide: Th17 and Treg cells in cancer and autoimmunity. *Cell Mol Immunol*. 2018;15(5):458–69.
  63. Dong C. TH17 cells in development: an updated view of their molecular identity and genetic programming. *Nat Rev Immunol*. 2008;8(5):337–48.
  64. Peng DH, Rodriguez BL, Diao L, et al. Th17 cells contribute to combination MEK inhibitor and anti-PD-L1 therapy resistance in KRAS/p53 mutant lung cancers. *Nat Commun*. 2021;12(1):2606.
  65. Herndler-Brandstetter D, Ishigame H, Shinnakasu R, et al. KLRG1(+) effector CD8(+) T cells lose KLRG1, differentiate into all memory T cell lineages, and convey enhanced protective immunity. *Immunity*. 2018;48(4):716–29.e8.
  66. Joshi NS, Cui W, Chandele A, et al. Inflammation directs memory precursor and short-lived effector CD8(+) T cell fates via the graded expression of T-bet transcription factor. *Immunity*. 2007;27(2):281–95.
  67. Hui Z, Ren Y, Zhang D, et al. PD-1 blockade potentiates neoadjuvant chemotherapy in NSCLC via increasing CD127(+) and KLRG1(+) CD8 T cells. *NPJ Precis Oncol*. 2023;7(1):48.
  68. Lou C, Wu K, Shi J, Dai Z, Xu Q. N-cadherin protects oral cancer cells from NK cell killing in the circulation by inducing NK cell functional exhaustion via the KLRG1 receptor. *J Immunother Cancer*. 2022;10(9):e005061.
  69. Nakamura S, Kuroki K, Ohki I, et al. Molecular basis for E-cadherin recognition by killer cell lectin-like receptor G1 (KLRG1). *J Biol Chem*. 2009;284(40):27327–35.
  70. Zeng J, Zhang L, Ma S, et al. Dysregulation of peripheral and intratumoral KLRG1(+) CD8(+) T cells is associated with immune evasion in patients with non-small-cell lung cancer. *Transl Oncol*. 2024;45: 101968.
  71. Patil NS, Nabet BY, Müller S, et al. Intratumoral plasma cells predict outcomes to PD-L1 blockade in non-small cell lung cancer. *Cancer Cell*. 2022;40(3):289–300.e4.
  72. Meylan M, Petitprez F, Becht E, et al. Tertiary lymphoid structures generate and propagate anti-tumor antibody-producing plasma cells in renal cell cancer. *Immunity*. 2022;55(3):527–41.e5.
  73. Germain C, Gnjatic S, Tamzalit F, et al. Presence of B cells in tertiary lymphoid structures is associated with a protective immunity in patients with lung cancer. *Am J Respir Crit Care Med*. 2014;189(7):832–44.
  74. Xiang X, Wang J, Lu D, Xu X. Targeting tumor-associated macrophages to synergize tumor immunotherapy. *Signal Transduct Target Ther*. 2021;6(1):75.
  75. Zhang H, Liu L, Liu J, et al. Roles of tumor-associated macrophages in anti-PD-1/PD-L1 immunotherapy for solid cancers. *Mol Cancer*. 2023;22(1):58.
  76. House IG, Savas P, Lai J, et al. Macrophage-derived CXCL9 and CXCL10 are required for antitumor immune responses following immune checkpoint blockade. *Clin Cancer Res*. 2020;26(2):487–504.
  77. Bill R, Wirapati P, Messemaker M, et al. CXCL9:SPP1 macrophage polarity identifies a network of cellular programs that control human cancers. *Science*. 2023;381(6657):515–24.
  78. Cords L, Engler S, Haberecker M, et al. Cancer-associated fibroblast phenotypes are associated with patient outcome in non-small cell lung cancer. *Cancer Cell*. 2024;42(3):396–412.e5.
  79. Li X, Sun Z, Peng G, et al. Single-cell RNA sequencing reveals a pro-invasive cancer-associated fibroblast subgroup associated with poor clinical outcomes in patients with gastric cancer. *Theranostics*. 2022;12(2):620–38.
  80. Ma C, Yang C, Peng A, et al. Pan-cancer spatially resolved single-cell analysis reveals the crosstalk between cancer-associated fibroblasts and tumor microenvironment. *Mol Cancer*. 2023;22(1):170.
  81. Sarode P, Mansouri S, Karger A, et al. Epithelial cell plasticity defines heterogeneity in lung cancer. *Cell Signal*. 2020;65: 109463.
  82. Cheung WK, Nguyen DX. Lineage factors and differentiation states in lung cancer progression. *Oncogene*. 2015;34(47):5771–80.
  83. Wang W, He J, Lu H, Kong Q, Lin S. KRT8 and KRT19, associated with EMT, are hypomethylated and overexpressed in lung adenocarcinoma and link to unfavorable prognosis. *Biosci Rep*. 2020;40(7):BSR20193468.
  84. Yuan X, Yi M, Dong B, Chu Q, Wu K. Prognostic significance of KRT19 in lung squamous cancer. *J Cancer*. 2021;12(4):1240–8.
  85. Han W, Hu C, Fan ZJ, Shen GL. Transcript levels of keratin 1/5/6/14/15/16/17 as potential prognostic indicators in melanoma patients. *Sci Rep*. 2021;11(1):1023.

## Publisher's Note

Springer Nature remains neutral with regard to jurisdictional claims in published maps and institutional affiliations.